A neutralizing antibody prevents post-fusion transition of measles virus fusion protein

Dawid Zyla, Roberta Della Marca, Gele Niemeyer, Gillian Zipursky, Kyle Stearns, Cameron Leedale, Elizabeth Sobolik, Heather Callaway, Chitra Hariharan, Weiwei Peng, et al.

A neutralizing antibody prevents post-fusion transition of measles virus fusion protein

Authors:

Dawid S. Zyla[1], Roberta Della Marca[2,3,4], Gele Niemeyer[1,5], Gillian Zipursky[2,3], Kyle Stearns[2,3], Cameron Leedale[6], Elizabeth B. Sobolik[7], Heather M. Callaway[1#], Chitra Hariharan[1], Weiwei Peng[8,9], Diptiben Parekh[1], Tara C. Marcink[2,3], Ruben Diaz Avalos[1], Branka Horvat[10], Cyrille Mathieu[11], Joost Snijder[8,9], Alexander L. Greninger[7], Kathryn M. Hastie[1], Stefan Niewiesk[6], Anne Moscona[2,3,12,13], Matteo Porotto[2,3,4*], Erica Ollmann Saphire[1,14*]

Affiliations:

[1]Center for Vaccine Innovation, La Jolla Institute for Immunology, La Jolla, CA 92037, USA

[2]Center for Host-Pathogen Interaction, Columbia University Vagelos College of Physicians and Surgeons, New York, New York, U.S.A.

[3]Department of Pediatrics, Columbia University Vagelos College of Physicians and Surgeons, New York, New York, U.S.A.

[4]Department of Experimental Medicine, University of Campania' Luigi Vanvitelli', 81100 Caserta, Italy

[5]University of Luebeck, Ratzeburger Allee 160, 23562 Lübeck, Germany

[6]Department of Veterinary Biosciences, College of Veterinary Medicine, The Ohio State University, Columbus, Ohio, USA.

[7]Department of Laboratory Medicine and Pathology Virology Division, University of Washington, Seattle, WA, USA.

[8]Biomolecular Mass Spectrometry and Proteomics, Bijvoet Center for Biomolecular Research and Utrecht Institute for Pharmaceutical Sciences, Utrecht University, Padualaan 8, 3584 CH, Utrecht, The Netherlands

[9]Netherlands Proteomics Center, Padualaan 8, 3584 CH, Utrecht, The Netherlands

[10]Immunobiology of Viral Infections, International Center for Infectiology Research-CIRI, INSERM U1111, CNRS UMR5308, University Lyon 1, ENS de Lyon, Lyon, France.

[11]Centre International de Recherche en Infectiologie équipe Neuro-Invasion, TROpism and VIRal Encephalitis (NITROVIRE), INSERM U1111 - Université Claude Bernard Lyon 1, CNRS, UMR5308, Ecole Normale Supérieure de Lyon, Université Lyon, Lyon, France

[12]Department of Microbiology & Immunology, Columbia University Vagelos College of Physicians and Surgeons, New York, New York 10032, United States

[13]Department of Physiology & Cellular Biophysics, Columbia University Vagelos College of Physicians and Surgeons, New York, New York 10032, United States

[14]Dept. of Medicine, University of California San Diego. La Jolla, California 92037 United States

[#] current address: Department of Chemistry & Biochemistry, Montana State University

***Correspondence should be addressed to: mp3509@columbia.edu and erica@lji.org**

Abstract (117 words):

Measles virus (MeV) presents a public health threat that is escalating as vaccine coverage in the general population declines and as populations of immunocompromised individuals, who cannot be vaccinated, increase. There are no approved therapeutics for MeV. Neutralizing antibodies targeting viral fusion are one potential therapeutic approach but have not yet been structurally characterized or advanced to clinical use. We present cryo-EM structures of pre-fusion F alone (2.1-Å resolution), F complexed with a fusion-inhibitory peptide (2.3 Å), F complexed with the neutralizing and protective antibody mAb 77 (2.6 Å), and an additional structure of post-fusion F (2.7 Å). *In vitro* assays and examination of additional EM classes show mAb 77 binds pre-fusion F, arrests F in an intermediate state and prevents transition to the post-fusion conformation. These structures shed light on antibody-mediated neutralization that involves arrest of fusion proteins in an intermediate state.

Introduction

Measles virus (MeV) is an enveloped, single-stranded negative-sense RNA virus that is highly transmissible (basic reproduction number (R_0) of 12-18) by the respiratory route. MeV belongs to the *Paramyxoviridae* family and causes considerable morbidity and mortality despite the availability of safe and effective MeV vaccines (*1, 2*). Measles accounts for more childhood deaths than any other vaccine-preventable disease. MeV was presumed to be eliminated in the U.S. (*i.e.*, ≥12 months without transmission) in 2000 (*1*). However, the reintroduction of the virus in recent years has resulted in a resurgence and repeated outbreaks (*2–6*). There were 9 million cases worldwide in 2021 (*7*), over 10.5 million in 2022, and between 2022 and 2023, the WHO European region observed more than a 30-fold increase in cases, with 40 of 53 member states affected (*8*). American vaccine coverage is now below the >95% required for herd immunity (see CDC reports (*9–18*)). Although outbreaks are usually attributed to the unvaccinated, cases also occur in people who were previously vaccinated (*6*, *19*, *20*). Up to 5% of vaccine recipients do not develop adequate protective antibodies, even after the recommended two-dose vaccination regimen, and even in those who do develop protective antibodies, vaccine-elicited immunity likely wanes over time (*21–26*). Even mild cases of measles infection can result in immune "amnesia" and loss of preexisting antibodies against other infections, leaving measles-convalescent individuals more vulnerable to future diseases (*27*, *28*). Rare, but severe complications of measles can lead to lethal MeV encephalitis (*29*, *30*).

MeV infects via coordinated action of the hemagglutinin (H) and fusion (F) envelope glycoproteins to mediate virus attachment to two cellular receptors, SLAM1/CD150 and Nectin-4, and entry into target cells (*31*). Vaccination results in neutralizing antibodies against these two proteins. Earlier work suggested that most neutralizing antibodies are directed against H and that anti-F antibodies elicited by the current vaccine are poorly neutralizing (*32–34*). A better understanding of the structures of F protein, the conformational changes of F that drive fusion, and whether antibody-mediated inhibition of conformational change can result in *in vitro* neutralization and *in vivo* protection against MeV are needed.

F is initially synthesized as a precursor molecule (F_0), which is subsequently cleaved into two subunits: the N-terminal F_2 and the C-terminal F_1. These subunits remain linked via a disulfide bond (35). Three F_1 and F_2 subunits assemble to form a pre-fusion F complex on the viral surface. This trimeric complex is kinetically trapped in the metastable state. Under physiological conditions, fusion activation requires the engagement of the H glycoprotein by the cell-surface receptor (*36–40*). Once this activation occurs, the pre-fusion F protein undergoes a substantial conformational change, elongating and embedding the hydrophobic fusion peptide into the membrane of the target cell. During the fusion process, F refolds into a stable 6-helix bundle post-fusion structure formed by the tight association of the N-terminal heptad repeat (HRN) and the C-terminal heptad repeat (HRC). This entire process brings the viral and cellular membranes in close proximity and leads to membrane merger (*41–48*). However, before adopting the low-energy post-fusion state, the F protein adopts a range of intermediate conformations, which require rearrangement of its domains.

Targeting the intermediate state of F is a potential antiviral approach. Although neutralizing monoclonal antibodies offer lifesaving treatments for several viruses, none are currently available to prevent or treat measles. Furthermore, no structural information is yet available for any antibody against MeV that could be used to define epitopes or activities that prevent or treat infection. The monoclonal antibody (mAb) for which structure and activities are documented here is one of the very few neutralizing mAbs described against the MeV envelope fusion (F) protein (*49*, *50*).

Results

Human chimeric mAb 77 potently inhibits MeV infection.

We previously isolated and sequenced an F-targeted neutralizing mouse antibody mAb 77.4 (*49*, *50*), and demonstrated that it inhibits MeV infection by blocking fusion (*49*). To facilitate future use as a human therapeutic, we grafted the 77.4 variable regions into a human IgG1 framework to obtain a chimeric antibody, now termed mAb 77, and assessed its *in vitro and in vivo* efficacy.

We first evaluated the antiviral activity of mAb 77 using an *in vitro* viral infection assay in which Vero-human CD150 (Vero-huCD150/SLAM) cells were treated with serial dilutions of mAb 77. Two distinct MeV F viral entry inhibitors were included as additional controls. One inhibitor, *N*-(3-cyanophenyl)-2-phenylacetamide (compound 3G in (*51*)), binds to prefusion F and blocks H-mediated fusion activation (*52*). The other inhibitor is an HRC-derived peptide termed HRC4, which binds to HRN in the pre-hairpin intermediate and blocks the conformational transition to the 6-helix bundle (*53*). After treatment, cells were infected with the MeV wt B3-eGFP virus. The mAb 77 potently inhibited infection with an IC_{50} of 0.034 nM (5.1 ng/mL) (**Fig. 1A**), which was substantially better than both HRC4 and 3G, which blocked fusion with IC_{50} values of 1.17 nM and 150.12 nM, respectively.

To test mAb 77 for *in vivo* efficacy against MeV exposure, we used the cotton rat model of measles virus infection (*54*, *55*). Cotton rats were treated with 0.1 mg/kg (n=5) or 1 mg/kg (n=10) of mAb 77 intraperitoneally 12 hours before challenge with 10^5 $TCID_{50}$ (*i.e.,* 50% tissue culture infectious) dose of MeV wt B3-GFP. Antibody pre-treatment resulted in a significant reduction in viral replication as compared to mock-treated animals that had an average titer of 3.6 log10±0.8 $TCID_{50}$/g lung tissue (**Fig. 1B**). Three of the animals pretreated with 0.1mg/kg mAb were virus negative, and two had reduced virus titers in lung tissue (2.4 and 2.6 log10 $TCID_{50}$/g lung tissue). Eight of the animals treated with 1 mg/kg mAb were virus-negative, and two had reduced virus titers (mean of 2.9 and 3.6 log10 $TCID_{50}$/g lung tissue).

mAb 77 prevents conformational changes required for fusion.

The F protein is primed to undergo substantial conformational change and refolding to drive the fusion of the viral and host membranes. These structural changes are triggered by a signal from the stalk region of the H protein, which is activated once the globular head of the H protein binds to its cellular receptor (*56*). As a first step in F conformational rearrangement, the N-terminal heptad repeat (contained in Domain III of the F1 head region) refolds from three short helices and beta-hairpin motifs into a single, approximately 100 Å-long helix. This assembled and now extended helix projects the fusion peptide, toward and into the host membrane. This extended F conformation is often called the 'pre-harpin intermediate' (*57*, *58*). The subsequent sequence of events remains elusive but, by analogy with other viruses, likely involves substantial rearrangement and repositioning of the stalk region containing the HRC. This movement enables the HRC to collapse onto the HRN into a 6-helix bundle that draws the viral and host membranes together to promote fusion.

Previous studies demonstrated that murine mAb 77.4 inhibits the fusion of viral and host cell membranes, but the step at which it functions remains unclear (*49*). The mAb 77 antibody could: (1) stabilize the F prefusion conformation to prevent F from triggering; (2) allow triggering but stabilize the intermediate state to prevent subsequent refolding and membrane fusion; or (3) impair F refolding by another mechanism.

To elucidate the stage of the fusion process at which mAb 77 acts, we used an assay that measures fusion between transfected HEK293T cells with red blood cells (RBC) by quantifying the amount of hemoglobin released upon lysis (**Fig. 2A and B)** (*53*). An integral component of this assay is the ability to release receptor engagement by H so that anchoring of RBCs by H can be distinguished from anchoring by F. As RBCs do

not display either of the MeV receptors for wt H (*i.e.*, CD150/SLAM or nectin-4), we instead employed a previously characterized chimeric protein that contains the MeV H stalk fused to the sialic acid receptor-binding head domain of paramyxovirus human parainfluenza virus 3 (HPIV3) HN (*53*). The interaction of the H-HN chimeric protein with the sialic acid displayed on the RBC surface can be reversed through treatment with the small molecule zanamivir (*59*, *60*). Hence, the H-HN chimera enables both reversible attachment to RBCs and MeV H-driven triggering of F. H-HN and F transfected cells were first incubated with RBCs at 4 °C to permit sialic acid binding but not fusion. The cell mixture was then treated with either media or different viral entry inhibitors, and fusion was allowed to proceed for 60 mins at 37 °C. Treatment with diluent media alone resulted in fusion of approximately 50% of total RBCs with the HEK293T cells (**Fig. 2A and B, Fig. S1A, B**). The remaining RBCs had either begun, but not completed, fusion (irreversibly bound through F) or had not yet initiated fusion (reversibly bound through HN only). Treatment with the 3G inhibitor prevented nearly all F-mediated anchoring, indicating, as previously reported, that this inhibitor prevents F activation(*53*, *61*). Meanwhile, treatment with the HRC4 peptide inhibitor resulted in most RBCs being irreversibly bound, indicating that F was activated but could not complete fusion, as previously described (*53*). Treatment with mAb 77 had the same effect as HRC4, where most RBCs were irreversibly bound but not fused. We conclude from these results that, unlike 3G, mAb 77 does not completely prevent the activation of F, nor does it inhibit the insertion of the fusion peptide into target cells. It does, however, prevent the collapse of the pre-hairpin intermediate into the 6-helix bundle required for fusion, suggesting that mAb 77 remains associated with an intermediate form of F.

Natural substitutions allow for production of MeV F in the pre-fusion state.

To structurally elucidate the mechanism of action of mAb 77, we first established a protein purification protocol using a stabilized MeV F construct. Expression of the wild-type MeV F ectodomain (amino acids 1-495) results in the production of F in its post-fusion conformation only. Previous structural characterization of MeV F was achieved by engineering four cysteines in the stalk region, which results in disulfide linkages between the three protomers (*52*). However, the protein produced from this construct aggregated, even at lower concentrations. As such, we instead generated a MeV F ectodomain that incorporates two naturally occurring point mutations, E170G and E455G (**Fig. 3A**). These mutations were derived from human central-nervous system isolates of MeV and stabilized F in the pre-fusion state (*62*, *63*). When paired, stabilization was further enhanced (**Fig. S2A, B**). This F ectodomain, termed F_{ECTO}, was ~95% cleaved by Furin, and approximately 85% of the resulting particles were in the pre-fusion conformation (**Fig. S2 C, D**). Mass spectrometry revealed that all three predicted N-glycosylation sites were occupied with oligomannose and (core-fucosylated) paucimannose glycans, as expected for the insect cell expression system (**Fig. S7C**).

Although F_{ECTO} can be purified in the pre-fusion state, the protein refolds to the post-fusion state over time. To determine how to maintain the pre-fusion conformation, we used differential scanning fluorimetry (DSF) to systematically explore the impact of pH and salt concentration on the apparent melting temperature (T_m^{app}) of F_{ECTO} (**Fig. S2 E, F**). Although pH had little influence on the T_m^{app} of F_{ECTO}, higher salt concentration increased the T_m^{app} from 44.6 °C to 54.8 °C, at 60 mM and 1460 mM NaCl, respectively (**Fig. S2 F**). Hence, buffering conditions of 800 mM NaCl and 50 mM HEPES pH 8.0 were used in the subsequent purification of F_{ECTO}. We saw no F_{ECTO} in the post-fusion conformation even after more than 2 weeks of storage in this buffer (**Fig. S2 B**).

Structure of pre-fusion F

We determined a 2.11-Å resolution cryo-EM structure of F in its unbound, pre-fusion state to investigate the influence of the introduced stabilizing mutations (**Fig. 3B, Fig. S3 A, S4 A, S5 A**). This high-resolution structure of the natural F_{ECTO} closely resembles the previous cysteine-stabilized prefusion F ectodomain with two exceptions (*52*). First, loop 248-265 adopts a different conformation likely attributable to previous crystal contacts **(Fig. S6A, B, C)**. Second, the alpha helices of the HRC in the ectodomain stalk resolved here begin to supercoil around each other starting at residue 473, whereas those in the Cys-stabilized construct remain linear and do not supercoil **(Fig. S6A, B, C)**.

Prefusion F in complex with inhibitor

We next solved the structure of F_{ECTO} in complex with $[FIP\text{-}HRC]_2\text{-}PEG_{11}$, a tandem peptide conjugate of two copies each of FIP-HRC, linked by a PEG_{11} moiety (*53*) (**Fig. 3C, Fig. S3 B, S4 B, S5 B**). As this inhibitor contains both FIP, which stabilizes prefusion F, and an HRC mimic, which binds to the pre-hairpin intermediate, it could theoretically capture either the pre- or post-triggered state of F, provided the correct state is available for binding. We obtained a high-resolution structure of the $F_{ECTO}\text{-}[FIP\text{-}HRC]_2\text{-}PEG_{11}$ complex at 2.3-Å resolution (**Fig. 3C, Fig. S3 B, S4 B, S5 B**). Similar to the previous structure of MeV Cys-stabilized F in complex with a related peptide inhibitor (*52*), here we find that FIP stabilizes F by occupying the hydrophobic pocket created by F1 residues from all 3 protomers, an interaction that locks MeV F in the prefusion state (*52*, *53*, *64*). All F_{ECTO} particles adopt a prefusion state with apparent density for FIP, but no density for the HRC-derived peptide **(Fig. S6 D, E)**. The lack of observable alternative conformations of F and the lack of HRC density together suggest that a fusion-intermediate state was not available for HRC to bind stably.

Prefusion F in complex with mAb 77

Our cell-based assays indicate that binding of mAb 77 locks F into an intermediate state of refolding, after release of the fusion peptide, but before collapse of the trimer into the 6-helix bundle required to complete fusion. The Fab of mAb 77 (Fab 77) binds F_{ECTO} with a K_D of 360 pM (0.36 nM) (**Fig. S2 E),** which is consistent with its potent *in vitro* neutralization. To elucidate the binding epitope of mAb 77 and further discern its mechanism of action, we obtained a F_{ECTO}-Fab 77 complex and determined its high-resolution by cryo-EM (**Fig. S2 F**).

The final map of the F_{ECTO}-Fab 77 complex was resolved to 2.6-Å resolution, showing three copies of Fab 77 binding to the prefusion F_{ECTO} trimer (**Fig. 3E, Fig. S3 C, S4 C, S5 C**). The antibody epitope lies at the base of the trimer and encompasses regions in both F1 and F2 from one protomer plus an additional F1 from a neighboring protomer (**Fig. 3 D, E, G**). The heavy chain of Fab 77 contributes the bulk of the interaction, burying 889 $Å^2$ of surface area on F_{ECTO}, whereas the light chain buries 106 $Å^2$ (**Table S2**). The predominant interactions between the antibody and F_{ECTO} occur via the heavy chain complementarity-determining region (CDR) 3, with additional contributions from CDR H1, CDR H2, and CDR L2 (**Fig 3G, Table S3**).

CDR H2 contacts $F2_A$ residues W27, G37, and S40. CDR H1 residues Y27 and S31 form hydrogen bonds with the backbone of residues L123 and V125, located in the fusion peptide of $F1_B$ in the neighboring protomer (**Fig. 3F**). Meanwhile, CDR-H3 occupies a shallow cleft between domains I and II of $F1_B$, forming six hydrogen bonds and one salt bridge. $F1_B$ residue R436 forms hydrogen bonds to the backbone oxygens of CDR H3 residues Y105 and Y107 and a salt bridge with CDR H3 D109 (**Fig. 3H**). CDR L2 residues Y49 and Q55 also bind to this region, making a hydrogen bond with the backbone nitrogen of $F1_B$ residue R435 and the hydroxyl group of S434 (**Fig. 3H, Table S4**). Together, this extensive network of 16 hydrogen bonds

and one salt-bridge anchor domains I and II of F1 in the prefusion state. Despite the glycan being closely located to the Fab 77 epitope at N29, no interactions were observed between Fab 77 and N29.

F post-fusion structure

Our structure of F_{ECTO} in complex with Fab 77 unequivocally demonstrates that this mAb recognizes the pre-fusion conformation of F and anchors the fusion peptide through interactions with CDR H1. However, our RBC fusion assay (**Fig 2**) suggests that mAb 77 prevents viral infection by arresting the fusion process after the fusion peptide has been released from the trimer and inserted into the host cell membrane.

To reconcile the structural finding that the Fab 77 epitope is in pre-fusion F, with the experimental data suggesting that the Fab 77 stabilizes a transitional state after activation, we determined the cryo-EM structure of MeV F in its post-fusion state. Direct structural comparison of the pre- and post-fusion states from the same protein sequence would provide a more comprehensive understanding of the conformational dynamics of F_{ECTO} and clarify how mAb 77 might selectively interact with the pre-fusion form or reveal conservation of the epitope in the post-fusion form.

As mentioned above, storage of F_{ECTO} in a high-salt buffer promotes conformational stability, whereas storage in a low-salt buffer induces spontaneous refolding to the post-fusion state. Hence, we incubated F_{ECTO} in low-salt buffer (*i.e.,* 150 mM NaCl) and solved a 2.7-Å resolution cryo-EM structure of its post-fusion conformation, using the same construct as represented in our pre-fusion F_{ECTO} structures (**Fig. 4 A, B**).

Like post-fusion structures of other paramyxovirus F proteins, the MeV F_{ECTO} post-fusion structure adopts a distinct elongated shape with a refolded head region and an extended 6-helix bundle composed of HRN and HRC (*41*, *65–68*), **Fig. 4A, B, Fig. S7A**). This conformational shift reduces the head radius by around 20% (from ~110 Å to ~93 Å) and extends the protein's long dimension by 60 Å (**Fig. S7 A, B**). The fusion peptide (FP, residues 115-140) is part of the F_{ECTO} sequence, but we could not observe the corresponding density for the fusion peptide, likely due to its inherent flexibility.

Alignment of the post-fusion structure of F_{ECTO} with its pre-fusion counterpart revealed that domain I (residues 290-373) and the N-terminal part of F2 have the lowest degree of rearrangement during fusion and provide a structural hinge about which the movement and rotation of other domains occur (*45*, *69*) (**Fig. 4C**). In contrast, domains II (F1 residues 374-426) and III (F1 residues 115-287 and F2 residues 50-104) show substantial spatial and structural rearrangement (**Fig. 4D, E, Fig. S7 B**). Although the majority of domain II retains the immunoglobulin-like fold present in the pre-fusion conformation, residues 434-446 of this domain, as well as the linker connecting domain II to HRC (residues 447-456), elongate as HRC transitions from the "down" state to the "up" state as fusion proceeds. As a result, all of domain II shifts 4.3 Å toward domain I.

The most profound conformational change between the pre- to post-fusion state occurs in the fusion peptide and HRN. Structural rearrangement within these regions includes refolding of HRN from several disjointed helices and β-strands to one elongated helix, exposure of the buried fusion peptide, and a 52° rotation around residue T287 (**Fig. 4D**). Overall, the conformational transition from pre- to post-fusion involves dramatic refolding of the fusion peptide and HRN, as well as retention of the globular domain structure with repositioning of the domains relative to their pre-fusion positions **(Movie 1)**.

The major conformational shifts and repositioning of the three distinct components of the tripartite mAb 77 epitope clarify why this antibody cannot recognize F in its post-fusion state (**Fig. 4F**). Specifically, the spatial rearrangement between domain II and the HRC, coupled with the movement of domain II relative to domain I, lead to the dislocation of the mAb 77 epitope and loss of recognition of post-fusion F.

Preservation of the mAb 77 binding interface in MeV variants.

Although MeV has been generally considered to be serologically monotypic, genetic characterization of wild-type viruses identified eight clades (A-H) that can be further divided into 22 genotypes plus one additional proposed genotype (*70–73*). To evaluate whether natural genetic variation in MeV might impact mAb 77 binding, we examined sequence conservation across the available MeV F protein sequences in the NCBI database. Of the 550 residues in MeV F, 319 are fully conserved among the variants, but 231 (42%) have single or multiple amino acid substitutions (**Fig. 5A, B)**. Within the mAb 77 epitope, however, only two residues, G37 and R436, vary across the range of known MeV sequences (**Fig. 5C**). The G37R mutation is extremely rare, occurring in only one instance (0.12% of sequences), but R436K occurs over 25% of F sequences. Binding of mAb 77 observed for wildtype F bearing an R436K mutation is similar, but mAb 77 did not bind F carrying the rare G37R mutation **(Fig. S8 A, B, C)**. In addition, the G37R mutation also decreased F-mediated fusion activity, which may be one reason for the low natural incidence of this substitution in circulating viruses (**Fig. 5D, Fig. S8D, E**).

mAb 77 interrupts the fusion cascade, leading to trimer disintegration.

Our structure of mAb 77 in complex with F, coupled with our post-fusion structure of F, clearly demonstrated that the epitope targeted by mAb 77 is specific to the prefusion conformation. However, our mechanistic fusion assay suggested that mAb 77 acts on F at an intermediate state, after F has been triggered and fusion activated, but before the 6-helix bundle has formed.

To further illuminate the mechanism by which mAb 77 inhibits viral entry, we investigated its impact on F_{ECTO} structure and stability. Specifically, we considered two (not mutually exclusive) hypotheses: (1) mAb 77 induces a conformational change in the epitope of F, potentially leading to the destabilization of the trimer, or (2) mAb 77 stabilizes both pre-fusion F_{ECTO} and an intermediate state, halting the refolding cascade from two arms. To test these hypotheses, we (a) compared the structure of F in the absence and presence of Fab 77 and (b) assessed the impact of Fab 77 on F thermal stability using differential scanning fluorimetry (DSF) and temperature-resolved dynamic light scattering (DLS). These complementary approaches enabled us to assess the overall stability of F and F-Fab 77 complexes (DSF) and monitor temperature-induced changes in protein conformation (DLS).

Alignment of the structures of F_{ECTO} alone and in complex with Fab 77 demonstrated high structural conservation, with a root-mean-square deviation (RMSD) of 0.75 Å over all Cα or 1.24 Å over all atoms (**Fig. S9 A**). Residues involved in the mAb 77 epitope showed only minor differences between structures, with fusion peptide residues L123 and V125 having an RMSD of ~2 Å over all atoms (**Fig. S9 A, B)**. Hence, binding of Fab 77 only marginally altered the conformation of F_{ECTO}.

DSF analysis demonstrated a modest increase in the thermostability of F when bound to Fab 77 (T_m^{app} of 47.6 °C vs. 51.6 °C in the unbound and bound state, respectively; **Fig. S9C)**. This stabilization was more limited than that seen for $[FIP\text{-}HRC]_2\text{-}PEG_{11}$ (56.2 °C), but nevertheless suggests that binding of mAb 77 does not inherently destabilize F_{ECTO}. Meanwhile, although DLS analysis also demonstrated that the temperature at which the F_{ECTO}-Fab 77 complex begins to unfold (i.e., T_m^{onset}) is similar to that of F alone, we found that the conformational behavior of the complex is markedly different (**Fig. S9D**). In the absence of Fab 77, the hydrodynamic radius (Rh) of F_{ECTO} is ~5.5 nm up to 44.7 °C, beyond which there is a steady temperature-dependent increase in Rh, likely reflective of the transition to the post-fusion state, followed by aggregation. Conversely, a clear plateau phase is observed for the F-Fab 77 complex, which remains arrested at an Rh of ~30 nm between 50 °C and 65 °C. This plateau is only surpassed above 65 °C, when Fab 77 presumably unfolds and releases F. These data suggest that mAb 77 only modestly enhances the stability of

prefusion F but readily inhibits its collapse to the post-fusion conformation through stable association with a fusion intermediate.

To visualize this potential intermediate(s) directly, we revisited our F_{ECTO}-Fab 77 cryo-EM dataset, this time incorporating previously rejected Fab-bound classes. Through extensive 2D classification, we identified several additional 2D class projections showing distinct Fab-induced F_{ECTO} conformations (**Fig. 6A**). Included in these projections was a complex of three Fabs bound to an F_{ECTO} trimer that is conformationally distinct from that of the prefusion trimer. In this case, a part of the head region appears to be drawn into the center of the F trimer, suggesting that a three-helix bundle would form upon release of the fusion peptide and refolding of the HRN. We additionally observed a class in which one F_{ECTO} protomer was dissociated from the trimer, leaving a "V"-shaped structure formed by the remaining two protomers, each bound by a Fab 77 molecule. Last, we identified a 2D class in which Fab 77 is bound to a small F_{ECTO} fragment (**Fig. 6A, B**). Similar 2D classes could be identified using time-resolved NS EM analysis, in which F_{ECTO}-Fab 77 complexes were incubated for 1-10 mins at 50° C before grid preparation (**Fig. S10, Fig. S11A**).

The scarcity of particles and views in the cryo-EM dataset hindered efforts to obtain 3D reconstructions for the trimeric refolding intermediate and separated protomer complexes. However, we successfully determined the structure of the Fab 77-stabilized F_{ECTO} fragment to 3.6-Å resolution (**Fig. 6C, Fig. S11B-F**). This structure reveals that Fab 77 is bound to F_{ECTO} domains I and II as well as the N-terminal segment of F2, in a manner similar to that of Fab 77 bound to prefusion F_{ECTO} (**Fig. S11G**). The lack of density for the fusion peptide suggests that this region has been released from the Fab 77 epitope, a possibility that is consistent with the results of our biochemical and cell-based assays.

Discussion

Most mAbs described thus far against measles virus are directed against the receptor-binding protein H (*74*). The limited set of mAbs identified for the fusion protein F fall into two principal antigenic categories, I and II (*50*). Category I mAbs are potently neutralizing, but susceptible to escape by naturally occurring MeV variants. Category II mAbs typically exhibit less potent neutralization and protection in mice, yet offer greater resilience against escape mutants. Where these antibodies specifically bind on the fusion protein is currently unknown, as the precise epitopes have not been characterized. mAb 77 (mAb 77) is category II but has high neutralization potency *in vitro* and protection *in vivo* (*49*, *50*).

Several antibodies that bind the pre-fusion state of other paramyxovirus fusion proteins have been described (*68*, *75–79*), and for the paramyxovirus respiratory syncytial virus (RSV), two such antibodies are in clinical use (*80–82*). In contrast to MeV, other paramyxovirus fusion proteins have three, rather than two, major epitope classes: the apex of the head domain, the trimer interface where two protomers meet, and the base of the head domain (**Fig S12 A-D).** Two mAbs that target Nipah virus F, 2B12 and 1H1, bind the base of the head domain that encompasses primarily domain II with single interactions with either domain I (2B12) or the cathepsin L cleavage site (1H1)(*68*). Here we show that mAb 77 against MeV also binds the base of the head domain, but its quaternary epitope spans across 3 domains and 3 polypeptide chains (**Fig 3F, H, Table S4**). We hypothesized that mAb 77, like the Nipah mAbs 2B12 and 1H1, inhibits viral entry by binding to pre-fusion F before it has been activated by H-receptor engagement on the target cell. This mechanism differs from that of HRC peptide mimics, which interact with the F protein only after activation of fusion when the virus has attached to the cell membrane, but before fusion has been completed (*83*, *84*). Unexpectedly, however, our mechanistic assays demonstrated that mAb 77 does not block any initiation of conformational change. Instead, like HRC mimics, mAb 77 allows initial triggering but arrests the protein at an intermediate step along the fusion pathway **(Fig. 2)**.

Curiously, the quaternary epitope of mAb 77 includes, at its edge, the fusion peptide of F, which extends from a neighboring protomer (*e.g.,* F_B) onto the top of domain II of F_A. However, the results of our mechanistic assay indicate that the fusion peptide is released and inserted into the host membrane, despite mAb 77 binding. We note that the fusion peptide makes a relatively small contribution to the overall epitope. Indeed, only two of the 16 hydrogen bonds between mAb 77 and F involve the fusion peptide (CDR H1 Y27 and S31 with L123 and V125, respectively). Based on PISA server predictions, these interactions contribute just -1.5 kcal/mol of free energy upon complex formation, in contrast to the -8.6 kcal/mol discharged across the entire epitope. Hence, the fusion peptide, located on the edge of the epitope, could potentially be extracted even though mAb 77 remains anchored to the N-terminal portion of F2 and the loop between domain II and HRC. The stronger remaining interactions would likely still preclude HRC repositioning, which requires release of the domain II-HRC loop. Furthermore, our structures suggest that the fusion peptide is not necessarily the first region to refold upon fusion triggering. Instead, the refolding of HRN from several disjointed sub-sections into an elongated helix could be the driving force for the refolding that, once initiated, pulls the FP from its location atop the neighboring domain II, like a ribbon from a box. This possibility is consistent with previous studies on refolding of the parainfluenza virus 5 F protein examined by oxidative foot-printing and mass spectrometry (*69*).

Based on these biochemical and structural findings, we propose a model of mAb 77-mediated protection against MeV that harmonizes our cell-based mechanistic studies with our biophysical and structural observations (**Fig. 6D**). In this model, (1) mAb 77 anchors F in a prefusion state through extensive interactions with two adjacent protomers. (2) Receptor engagement by H triggers refolding of F-HRN, and release of the fusion peptide from the mAb 77 epitope. (3) Continued binding of F by mAb 77 prevents complete refolding by anchoring F2 to domains I, II, and the linker in between. As a result, the binding of mAb 77 arrests an intermediate between pre and post-fusion states.

It is not yet clear whether mAb 77-mediated stabilization of prefusion F would completely inhibit F triggering in a natural viral infection or if the primary mechanism of action for this mAb is to prevent the completion of fusion. Our temperature-dependent DSF and DLS experiments demonstrated that mAb 77 enhances the stability of prefusion F up to ~50 °C, after which the complex adopts a conformational species distinct from that of apo-F. Meanwhile, our RBC-fusion assays indicated that F is activated at 37 °C, even in the presence of mAb 77. These seemingly contradictory results may be explained by the stabilizing mutations present in recombinant F_{ECTO} used for DSF and DLS experiments versus the destabilized, full-length F used in the cell-based assay. It is also unclear whether the intermediate states captured by NS- and cryo-EM reflect the structural trajectory of apo-F or if they are distinct states induced or enforced by mAb binding. Nevertheless, our analyses demonstrate that in addition to stabilization of pre-fusion F, mAb 77 also prevents fusion by remaining bound to a post-triggered F.

This dual mechanism of antibody-mediated defense may also apply to other antibodies that are specific for pre-fusion states. Several previous studies focusing on similar antibodies against Nipah, Hendra, or parainfluenza viruses have primarily examined binding kinetics, neutralization efficiency, and structure, but did not extensively explore mechanisms of activity. As a contrasting case, we have shown that the HPIV3-neutralizing antibody PIA174 stabilizes the pre-fusion state of the protein (*78*). The only other antibodies shown to recognize a refolding intermediate state of a viral fusion protein are the HIV-1 gp41-specific monoclonal antibodies, 2F5 and 4E10. These rare antibodies were known to neutralize by targeting a transient conformation during gp41-mediated membrane fusion. However, structures illuminating their specific binding to the intermediate state are as yet unresolved (*85*). The structures presented here, of the beginning and ending states of MeV F at high resolution, with additional lower-resolution views of captured intermediates along the path, illuminate a mechanism of neutralization by conformational arrest of the fusion protein at an intermediate, post-triggered state. This work paves the way for the next generation of measles virus therapeutics and illuminates a mechanism that may be shared by antibodies against other viral pathogens.

Materials and Methods

Plasmids

The genes of Measles morbillivirus (MeV) strains IC323 or B3 hemagglutinin protein (H), fusion protein (F), human nectin 4, and human CD150 (huCD150/SLAM) proteins were codon optimized, synthesized, and sub-cloned into the mammalian expression vector pCAGGS (Epoch Life Science). A codon-optimized F protein sequence derived from the Measles virus strain Ichinose-B95a (Taxonomy ID: 645098) was synthesized by GenScript and subcloned into the pcDNA3.1 vector. Stabilizing point mutations (E170G and E455G) previously characterized in SSPE and MIBE measles strains were sequentially introduced using the Q5 Site-Directed Mutagenesis kit (NEB). The ectodomain construct was generated by removing the transmembrane region and cytoplasmic tail residues (496-550) using the Q5 Site-Directed Mutagenesis kit. To generate *Drosophila* S2 stable cell lines, the F protein ectodomain construct E170G/E455G (F_{ECTO}) was subcloned from the pcDNA vector to the pMT-puro vector, including a C-terminal enterokinase cleavage site and a dual StrepII tag via NEB HiFi DNA assembly.

Cells

HEK293T (human kidney epithelial), Vero, and Vero- huCD150 (African green monkey kidney) cells were grown in Dulbecco's modified Eagle's medium (DMEM; Life Technologies; Thermo Fisher Scientific) supplemented with 10% fetal bovine serum (FBS, Life Technologies; Thermo Fisher Scientific) and antibiotics at 37°C in 5% CO_2. The Vero-huCD150 culture medium was supplemented with 1mg/ml of geneticin (Thermo Fisher Scientific). Drosophila S2 cells were cultured at 25°C without CO_2 in complete Schneider's Drosophila Medium (Gibco) supplemented with 10% heat-inactivated fetal bovine serum (FBS) and 1% penicillin-streptomycin (100 U/mL penicillin and 100 µg/mL streptomycin) or in serum-free Lonza Insect Xpress Medium. ExpiCHO cells were maintained in ExpiCHO Expression Medium (Gibco) supplemented with 8 mM L-glutamine in a humidified incubator at 37°C with 8% CO_2.

In vitro viral infection

Vero- huCD150 cells were plated in 96-well plates (1×10^4 cells/well). The following day, cells were treated with serial dilutions of monoclonal antibody 77 (mAb 77); N-(3-cyanophenyl)-2-phenylacetamide, referred to as 3G; or MeV F-derived HRC4 dimeric fusion inhibitory lipopeptide (*i.e.,* $[HRC\text{-}PEG_4]_2$-chol). Simultaneously, cells were infected with MeV wt B3-eGFP for 3 h at 37°C (150-200 pfu/well). After 3 h, the medium was replaced with medium containing 2% of methylcellulose Avicel/2× complete medium (1:1). After 24 h, eGFP-infected cells were counted using a Cytation 5 (BioTek) and analyzed with Gen5 3.11 software (min object size 25 µm, max object size 135 µm, threshold 3,000). The samples were tested in three experiments performed with technical duplicates in five-fold dilutions of 96-well plates. The measurements from each plate were normalized using 100 nM of mAb 77, 25 µM of 3G compound, or 500 nM concentration of HRC4 as 100% inhibition. Data was analyzed in OriginPro 2023, where all biological and technical replicates were globally fitted with logistic regression function with shared IC_{50} and Hill slope values, and A1 and A0 (highest and lowest signals) were used to normalize the data. Based on the normalized data, percent inhibition was calculated using the following equation: [1 - X]*100, where X is the fraction of the normalized signal.

Beta-Galactosidase (Beta-Gal) complementation-based fusion assay

The Beta-Gal complementation-based fusion assay was performed as previously described (*53*, *60*). Briefly, HEK293T cells transiently transfected with nectin 4 or huCD150 and the ß-Gal omega subunit are mixed with cells co-expressing glycoproteins F and H and the ß-Ga alpha subunit. Cell fusion leads to alpha-omega complementation and is measured in the presence or absence of fusion inhibitory compounds. Fusion is stopped by lysing the cells and, after addition of the substrate (®The Tropix Galacto-Star™ chemiluminescent reporter assay system, Applied Biosystems), fusion is quantified on either a Tecan M1000 microplate reader or a Biotek Cytation 5. Three biological replicates were recorded, and globally fitted with a logistic function in OriginPro 2023. Obtained parameters were used to normalize the data per sample and plotted with standard error calculated from all data points.

Cell surface staining with conformation-specific anti-F mAbs

HEK293T cells were transiently transfected with viral glycoprotein constructs. The transfected cells were incubated at the temperatures and times indicated in the figures. Specific MeV F conformations were detected with mouse mAbs followed by Alexa-488 anti-mouse secondary antibody (Life Technologies) and DAPI (4′,6-diamidino-2-phenylindole; Thermo Fisher) staining. Plates were imaged with a Cytation5, and the relative fluorescence of antibody-bound cells was determined using BioTek Gen5.

Viral rescue

HEK293T cells were transfected using Lipofectamine 2000 in 6-well plates coated with poly-D-lysine. The transfection mixture included cDNA constructs coding for viral proteins N (GS6558900-1), P (GS59482), and L (GS58944), all sourced from Epoch Life Science according to our design specifications. Additionally, cDNA for T7 polymerase (GS58929) and the genome for the MeV B3 eGFP wt virus (GS68838) were included. Cells were incubated overnight at 37°C in Opti-MEM medium. The medium was then replaced with DMEM supplemented with 10% FBS. Cells were then subjected to a heat shock treatment by incubating them at 42°C in a water bath for 3 h. Subsequently, the cells were returned to 37°C for 48 hrs. The cells were then detached and co-incubated with Vero-huCD150 cells in T75 flasks to facilitate rescued virus amplification. The virus underwent four passages and was titrated to a concentration of 10^6 plaque-forming units per milliliter (PFU/ml). The virus sample was then sequenced and used in subsequent *in vitro* and *in vivo* experiments.

In vivo experiments: Cotton rats

Inbred cotton rats (*Sigmodon hispidus*, cotton rat strain “Hsd:Cotton Rat” without genetic modifications) were purchased from Envigo, Inc., Indianapolis. Male and female cotton rats aged 5 to 7 weeks were used for experiments. For intranasal infection, 10^5 $TCID_{50}$ of MeV (strain B3 wt eGFP) was inoculated intranasally to isoflurane-anesthetized rats in a volume of 100 µl. Animals received intraperitoneally either the indicated amount of mAb 77 or vehicle 12 hrs prior to infection. Four days after infection, animals were euthanized by CO_2 inhalation, and their lungs were collected and weighed. Lung tissue was homogenized with a glass dounce homogenizer. Supernatants were serially diluted and titrated for infectious virus on Vero-huCD150 cells in 48-well plates. Plates were scored microscopically for cytopathic effect (CPE) after 7 days, and the tissue culture infectious dose 50 ($TCID_{50}$) was calculated. The results are presented as $TCID_{50}$/g of lung tissue.

Red Blood Cell (RBC) fusion assay

To investigate the specific stage at which mAb 77 affects the fusion process, we used a previously characterized assay involving RBCs and HEK293T cells transfected with a chimeric version of MeV H and MeV F bearing a T461I mutation (*53*, *60*). The chimeric version of H (termed H-HN) contains the stalk region of MeV H to maintain interaction with MeV F fused to the sialic acid receptor-binding domain of human parainfluenza virus 3 (HPIV3) HN protein. The interaction between H-HN and sialic acid receptors on RBCs can be reversed through treatment with zanamivir, which enables the differentiation of F-mediated anchoring from H-mediated anchoring. The T461I mutation was introduced into the F protein to reduce its stability and enhance fusion activation. Each of these specific proteins have been used in previous studies (*53*, *60*).

Transfected HEK 293T cells were incubated with a 1% v/v of RBCs in CO_2-independent media for 30 min at 4°C to allow for receptor binding without initiating the fusion process. Following this incubation period, the cells were washed three times with serum-free medium to remove unbound RBCs. The cells were then exposed to either diluent medium or mAb 77. MeV-F targeted inhibitors with known functions were also included as controls. These included the compound 3G (*N-(3-cyanophenyl)-2-phenylacetamide*), which prevents H-mediated fusion activation by binding to prefusion F (*51*), and a peptide derived from the heptad repeat C (HRC) region, named HRC4 (*83*), which obstructs the conformational transition necessary for fusion by interacting with the heptad repeat N (HRN) in the pre-hairpin intermediate state.

Following these treatments, the cell mixtures were warmed to 37°C for 60 min to activate F-mediated fusion of the RBCs and 293T cells. The outcomes of these interactions were classified into three groups: 1) reversibly bound RBCs; 2) irreversibly bound but not fused RBCs; and 3) RBCs that had successfully fused with HEK293T cells. Each population was quantified through measurement of hemoglobin as detailed below (see also **Fig. S1A** for an experimental schematic).

The assay is performed in poly-D-lysine biocotated 24-well plates on which HEK 293T cells are plated and transfected with the viral glycoproteins. The plates are then treated overnight at 37ºC with 25 mU/well of exogenous neuraminidase to prevent cell-to-cell fusion and maintain an intact cell monolayer. The following day, the plates are transferred to melting ice (4ºC) for 30 minutes, washed with cold CO2-independent media, and then incubated with RBCs (1%v/v) for 30 minutes. After this incubation, the unbound RBCs are washed from the cell surface, the treatments are added, and the cells are incubated at 37oC. Afterward, the plates are transferred to melting ice (4ºC) for assessment of the different populations of RBCs (reversibly bound, irreversibly bound, and fused). Reversibly bound RBCs (group 1) were separated from the cells expressing the viral glycoproteins by treating the wells with 10mM zanamivir for 30 mins at 4ºC. The addition of zanamivir allows the resuspension of the RBCs in the supernatant fluids, whereas the cells expressing the viral glycoproteins remain attached to the plastic in the well. The supernatant fluids containing the reversibly bound RBC were moved in V-bottomed 96-well plates and spun down. The RBCs remained at the bottom of the V-bottomed well and the supernatant was removed and replaced with ACK-Lysing buffer (ammonium-chloride-potassium, from Gibco A10492-01) to released in solution the hemoglobin. Irreversibly bound RBCs (group 2) were measured by incubating the cells (minus the removed, reversibly bound RBCs) with ACK-Lysing buffer (ammonium-chloride-potassium, from Gibco A10492-01) for 30 mins at 4°C. ACK buffer selectively lyses (unfused) RBCs by disrupting the internal ionic balance, resulting in the release of hemoglobin directly into the media. The hemoglobin is released in the supernatant fluids that are transferred to 96-well plate for hemoglobin quantification. The remaining cells (still bound to the plastic in the well) are fusions of RBC and HEK 239Ts (group 3) and are

ACK buffer insensitive. To release the hemoglobin, this population of cells were lysed with 50 mM HEPES (Gibco Cat#15630080), 100 mM NaCl, and 5 mg/mL dodecyl maltoside (Thermo Scientific Cat#89903) (DH buffer) and clarified via centrifugation. Lysate was then moved to flat-bottomed 96-well plates for hemoglobin quantification.

The level of hemoglobin was quantified for each group by measuring the absorbance of each lysate at 410 nm. The amount of hemoglobin in each group was added together to represent 100%. Each group is displayed as a fractional proportion of this normalized value.

F_{ECTO} purification

Drosophila S2 cells were transfected with a plasmid encoding the F ectodomain construct (pMT-puro-F_{ECTO}2M-EK-twin-Strep-TagII) following the manufacturer's protocol (referred throughout the text as F_{ECTO} for simplicity). On day 1, S2 cells were seeded in a 6-well plate (1.0×10^5 – 1.5×10^5 cells/mL) in 3 mL of complete Schneider's medium. On day 2, the cells were transfected with 2 µg of the plasmid using the Effectene (QIAGEN) transfection protocol. Selection with puromycin (6 µg/mL) started on day 5, at which point cells were transferred to a T25 flask. The cells were then gradually expanded to a T75 flask, with the medium replaced by Lonza Insect Xpress medium containing 6 µg/mL puromycin. Subsequently, cells were expanded to 2 x 1 L in 2 L shaking flasks, induced with 500 µM CuSO4 at 1×10^7 cells/mL, and harvested four days post-induction. Cells were removed from the culture medium by centrifugation at 5,000 x g for 20 min. The medium was adjusted to pH 8.0 with 1 M HEPES, and Biolock (IBA) (2.4 mL/L of medium) and NaCl (to a final concentration of 800 mM) were added. The medium was loaded onto a StrepTrap HP 5 mL column (Cytiva), and the column was washed with high-salt HBS (50 mM HEPES pH 8.0, 800 mM NaCl) until a stable UV absorbance at 280 nm was achieved. The protein was then eluted with high-salt HBS containing 5 mM d-desthiobiotin (Sigma). Next, the eluted protein fractions were pooled, and the buffer was exchanged for high-salt HBS using a HiPrep 26/10 Desalting column (Cytiva). Finally, the purified protein was flash-frozen in liquid nitrogen. Protein concentration was estimated using the molar extinction coefficient at 280 nm (48,820 M^{-1} cm^{-1}).

Antibody expression

Monoclonal antibody 77 (mAb 77) was produced in ExpiCHO cells by following the manufacturer's high-titer transfection protocol using the pTRIOZ-mAb 77 plasmid, which encodes the antibody heavy and light chains. After seven days of expression, cells were removed from the culture medium by centrifugation at 4,000 x g. The medium was then adjusted to pH 8.0 with 1 M HEPES (pH 8.0) and incubated overnight at 4°C with protein A agarose beads to capture the mAb 77. On a subsequent day, the beads were washed with 20 ml of HBS, and the bound antibody was eluted using 15 mL 0.2 M glycine (pH 2.0). The eluate was immediately neutralized by adding 10% (v/v) 1 M HEPES (pH 8.0).

To generate antibody fragments (Fabs), mAb 77 was digested at 1 mg/ml with 1% (w/v) cysteine-activated papain for 4 h at 37°C in a water bath. The enzymatic reaction was halted by adding 0.5 M iodoacetamide to a final concentration of 50 mM. Following digestion, the reaction mixture was diluted 10-fold with 10 mM HEPES (pH 8.0) to decrease salt concentration and loaded onto a 1 mL Mono S column pre-equilibrated with 20 mM HEPES (pH 8.0). The Fabs' flowthrough was collected, and the Fc fragments were eluted using a single step with 20 mM HEPES (pH 8.0) containing 2 M NaCl. The isolated Fabs were concentrated, and their buffer was exchanged for HBS. The Fabs were stored at 4°C for further analysis and

experimentation. Protein concentration was estimated using the molar extinction coefficient at 280 nm (mAb 77: 240360 M^{-1} cm^{-1}, Fab 77: 84,270 M^{-1} cm^{-1}).

Formation of F_{ECTO}-Fab 77 Complex

The F_{ECTO} and Fab 77 complex was prepared by incubating approximately 5 μM of F_{ECTO} with a three-fold molar excess of Fab 77 at 4°C overnight in HBS (50 mM HEPES, pH 8.0, and 150 mM NaCl). Following the incubation, the mixture was subjected to size-exclusion chromatography using a Superdex 200 Increase 10/300 GL column (Cytiva) in HBS. The fractions containing the F_{ECTO}-Fab 77 complex were collected, concentrated, and used on the same day.

Differential Scanning Fluorimetry (DSF) Assay

Differential Scanning Fluorimetry (DSF) was used to determine protein stability and evaluate variations in thermal denaturation profiles under distinct buffer conditions (*86*). Each analysis was conducted using 25 μL containing 2.5 μg of protein and 2.5 μL of a 1% SYPRO Orange solution (Thermo Scientific), with the remaining volume composed of the buffer being tested. Stability measurements for F_{ECTO}, F_{ECTO}-Fab 77, F_{ECTO}-$[FIP\text{-}HRC]_2$-PEG_{11} (described in (*53*)) were performed in HBS. For pH screening, buffers contained 50 mM Sodium Acetate (pH 5.0), Bis-Tris (pH 6.0), MOPS (pH 7.0), HEPES (pH 8.0), or CAPSO (pH 9.0). The salt screening was performed using 50 mM HEPES (pH 8.0) with NaCl concentrations ranging from 0 to 2 M.

The samples were dispensed into a 96-well PCR plate (BIO-RAD Multiplat 96-Well PCR Plates, low profile, unskirted), and the plate was then sealed (Bio-RAD Microseal 'B' PCR Plate Sealing Film) to prevent evaporation during the heating process. A thermal cycling procedure was initiated on a Bio-Rad CFX 96 thermocycler, with the temperature incrementally elevated from 25°C to 95°C at a rate of 1°C per min.

Throughout thermal cycling, SYPRO Orange fluorescence was monitored continuously with the wavelengths for excitation and emission set at 520 nm and 540 nm, respectively. Data analysis was automatically carried out in Bio-RAD CFX Manager software, and the first derivative of the melting curve was graphed against temperature. Each experimental condition was performed in quadruplicate, and the average derivative signal was calculated. The averaged derivative signal minimum represented the protein's apparent melting temperature (T_m^{app}).

Dynamic light scattering

Dynamic Light Scattering (DLS) experiments were performed using a Dynapro PlateReader-2 (Wyatt) instrument with Corning 384-well plates with clear bottom. Four independent replicates were recorded for each sample, and 25 μL of protein at 0.05 mg/ml was added to each well. The temperature ramp was set to increase at 0.2°C per min from 25 °C to 70 °C, resulting in a 1 °C ramp per cycle. The autocorrelation function for each replicate was fitted using regularization fit in DYNAMICS 7.8.1.3 software (Wyatt), and the radius of the dominant mass species was plotted against temperature. 10% of the total signal change was used to calculate the temperature onset, which was manually estimated for the obtained curves. For the Fab 77 fitting, the maximum signal was fixed at double the last measured point. The resulting plots were generated using Matplotlib.

Bio-layer interferometry

BLI-based kinetic analysis was conducted using the OctetRed384 system (Sartorius). Anti-human Fab (FAB2G, Sartorius) capture sensors were loaded with Fab at 15 µg/mL in 10 mM HEPES (pH 7.4), 150 mM NaCl, 3 mM EDTA, 0.05% Tween-20, 0.5 mg/ml BSA (1xHBSTE/BSA). Binding of F_{ECTO} to Fab-loaded sensors was performed using two-fold serial dilutions of F_{ECTO}. Baseline and dissociation steps were carried out in 1xHBSTE/BSA. Regeneration was carried out using 10 mM Glycine (pH 2.5). Reference sensors (those not loaded with Fab but dipped into F_{ECTO}-containing wells) were subtracted from each dataset to account for non-specific F_{ECTO} binding. Fab-only sensors were used as sample references. Kinetic parameters (K_{on} and K_{off}) and affinities (K_D) were calculated from a nonlinear fit based on the 1:1 binding kinetic model of the data using the Octet Data Analysis HT software version 11 (Sartorius). Three replicates for each binding curve were performed.

Structural mapping of protein variants

The sequences for MeV F proteins were acquired using a custom Python script using the BioPython library (*87*). This script was used to query the Entrez protein database for "Measles morbillivirus Fusion." All results obtained from this process were consolidated into a single FASTA file.

The sequences were then filtered based on size, retaining only those longer than 400 and shorter than 600 amino acids. Subsequently, the Needleman–Wunsch algorithm inside BioPython was employed for pairwise alignment with the F wt sequence (Uniprot: Q786F3) to curate the sequences further. Any sequences with low alignment scores (lower than 0) were removed from consideration.

After this curative process, the filtered FASTA file was globally aligned using the Clustal Omega software (*88*). This global alignment was stored in a clustal format file, which was then used to calculate the sequence conservation for each position using the AL2CO program (*89*). Primary sequence conservation was visualized and graphed using Matplotlib and Seaborn Python packages (*90*, *91*).

Structural sequence conservation was mapped onto the pre- and post-fusion structures of F_{ECTO} using ChimeraX 1.6, which also uses AL2CO (*92*). Statistics regarding the point mutations at the mAb 77 epitope were computed in Python based on the Clustal alignment.

Cell Surface Biotinylation

HEK 293T cells were seeded in a 6-well plate and transfected with measles B3 F proteins (wildtype-wt, 436K, 436G, 436D, 37R) or measles H, by mixing 2 µg/well of plasmid in OPTIMEM with 4 µg/well of Lipofectamine 2000 (Invitrogen Cat#11668019) in OPTIMEM (Gibco Cat#31985088) for 20 min at room temperature and incubating with cells for 3 hrs at 37 °C. After transfection, cells were incubated with DMEM (Gibco Cat#10569044) with 10% FBS (Gibco Cat#16000044) and 1% Penicillin-Streptomycin (Gibco Cat#15140122) at 37 °C or 32 °C for 24 or 48 hrs. Cells were then incubated at 4 °C with 3.3 mM NHS-S-S-dPEG$_4$-biotin (Quanta Biodesign Cat#10194) in DPBS (Gibco Cat#14287080) for 1 hr before lysing with DH Buffer [50 mM HEPES (Gibco Cat#15630080), 100 mM NaCl, 5 mg/mL dodecyl maltoside (Thermo Scientific Cat#89903) in Milli-Q Water] supplemented with cOmplete Protease Inhibitor Cocktail (1 tablet/50 mL; Roche Cat#11836145001). Biotinylated proteins were incubated with Streptavidin Sepharose beads (Invitrogen 434341) for 16 hrs at 4° C. Protein was eluted from washed beads in reducing Laemmli SDS Sample Buffer (Boston BioProducts Cat#BP-110R), boiled for 10 min, and run on a 4-20% Novex Tris-Glycine Protein Gel (Invitrogen Cat#WXP42026BOX). The gel was transferred to nitrocellulose using an iBlot quick transfer method (Invitrogen IB23001). The membrane was blocked (Invitrogen

Cat#WB7050), treated with Anti-Measles F HRC (GenScript; Rabbit) and alkaline phosphatase-conjugated anti-rabbit secondary antibody (Invitrogen Cat#WB7105). The blot was then developed using NBT/BCIP Substrate (Invitrogen Cat#WP20001). Analysis of the blot was performed with GelAnalyzer 23.1 and the integrated intensity of the bands was normalized to the expression level of F wt at 37 °C.

Grid preparation

Negative stain

Copper grids (400 mesh) coated with carbon film (CF400-Cu, Electron Microscopy Sciences) were used for negative staining. The grids were first subjected to glow discharge treatment using the easiGlow Glow Discharge Cleaning System (Pelco) for 15 sec at 15 mA to enhance hydrophilicity. Next, the protein sample concentration was adjusted to 0.01 absorbance units at 280 nm, and 3 µL of the sample was applied to the grid for a 1 min incubation. Subsequently, the grid was blotted to remove an excess sample and washed three times with 3 µL deionized water, blotting between each washing step. The grid was incubated with 3 µL 1% uranyl acetate solution for negative staining. After two blotting steps, a final drop of the staining solution was added, followed by a 1 min incubation. The grid was then blotted once more to remove excess stain and allowed to air-dry.

Graphene oxide grids

Graphene oxide (GO) grids were prepared in-house by diluting a commercial GO solution (2 mg/mL, Sigma-Aldrich) in deionized water to a final concentration of 0.2 mg/mL. This diluted solution was sonicated for 5 min in a water bath to ensure proper dispersion of GO layers. Next, large aggregates were removed via centrifugation at 500 x g for 1 min. Finally, the supernatant containing the dispersed GO was collected by transferring the upper 50% solution to a fresh 1.5 mL microcentrifuge tube.

Quantifoil R2/2 grids were washed with ethyl acetate overnight and glow-discharged under the same conditions as the negative stain grids. Then, 3 µL of the GO solution was applied to the grids and incubated for 4 min. The grids were blotted, rinsed with 20 µL deionized water, blotted once more, and air-dried for at least 10 min.

On the same day of grid preparation, dried GO grids were used for protein sample vitrification. The Vitrobot Mark IV plunge-freezing system was operated at 4 °C and a relative humidity of 100%. A 3 µL aliquot of the protein sample (0.2 – 0.5 mg/mL) was deposited onto the GO grid, followed by a 12 sec incubation period. After the incubation, the excess sample was blotted away (blot force 0) for 3 sec. The grid was immediately plunge-frozen in liquid ethane cooled by liquid nitrogen.

C-flat grids

C-flat 1.2/1.3 400 mesh grids were glow discharged and immediately used for sample freezing. A 3 µL aliquot of 0.5 mg/mL protein sample was deposited onto the grid, immediately blotted for 6 sec, and plunge-frozen in liquid ethane cooled by liquid nitrogen.

Cryo-EM data processing

F_{ECTO}-Fab 77

Movies were collected on a Titan Krios operated at 300 KV using a K3 Direct electron detector (Gatan) in counting mode (0.66 Å $pixel^{-1}$) at a nominal magnification of ×130,000 using a defocus range of −0.5 µm to −2.0 µm with the BioQuantum energy filter slit set to 20 eV. Movies (LZW compressed TIFF files) were

collected in EPU (Thermo) over a 3 sec exposure with an exposure rate of ~15 e− pixel^{-1} sec^{-1}, resulting in a total exposure of ~50 e− Å^{-2} (1 e^{-} Å^{-2} frame^{-1}). Downstream processing was done using Relion, homemade Relion scripts (https://github.com/dzyla/cryoem_notebook; https://github.com/dzyla/Follow_Relion_gracefully), and cryoSPARC (*93–96*). Frame alignment was done in Relion 4 using MotionCor2 version 1.4.0 with 6x5 patches and a B factor of 150 (*97*). CTF determination was performed using CTFFIND4 version 4.1.14 using dose-weighted micrographs (*98*).

Particles were auto-picked in Relion from randomly selected micrographs using the Laplacian-of-Gaussian algorithm, extracted at 512 px box size and Fourier-cropped to 64 px (5.28 A/px), and used for the 2D classification step. Next, particles resembling glycoprotein were selected and subjected to further rounds of 2D classification. The best classes showing different glycoprotein orientations were selected and used for Topaz model training over 10 epochs with ~10,000 particles (*99*). Finally, the optimized model was used to pick particles in the whole dataset. Approximately 1.1M particles were extracted in Relion, imported into cryoSPARC, and subjected to 2 rounds of 2D classification. Classes resembling glycoprotein with bound Fab were selected (148,000 particles), and particles corresponding to Fab only were discarded. Selected particles from cryoSPARC were transferred back to Relion using a homemade script and re-extracted at 512 px with Fourier-cropping to 160 px (2.112 A px^{-1}). Particles were again imported to cryoSPARC, where the initial model was generated. The obtained model was used for the 3D classification in Relion with 3 classes.

During the first 25 iterations, global angular searches were performed using 15° sampling intervals. Once the classification reached equilibrium (followed by monitoring class distribution using Follow Relion Gracefully (*96*)), the 3D classification job was resumed with local angular searches of 7.5° sampling intervals and a 30° local angular search range. This procedure was repeated with a decreasing angular sampling interval and search range (kept double the angular sampling) until there was no improvement in estimated angle accuracy. Two classes showed high-resolution features and were selected for the 3D Refine protocol (142,000 particles). Next, refined particles were re-extracted at 512 px with Fourier-cropping to 320 px (1.056 A px^{-1}) with recentering coordinates. Finally, particles were refined, post-processed, and CTF and aberration refinement were performed. This procedure was repeated until there was no improvement in the reported post-processing resolution. Then, the Polishing step was applied, first by training on 10,000 particles with the fraction of Fourier pixels for testing set to 0.5. The obtained trained parameters were used for particle polishing, and particles were extracted at 320 px (1.056 A px^{-1}). Particles were again 3D refined, and CTF and aberration refinement were performed until there was no further improvement in the reported post-processing resolution. Finally, polished particles were imported into cryoSPARC, and a non-uniform refinement protocol was used to generate the final cryo-EM map in C3 symmetry. Then, particles were C3 symmetry expanded and refined using the Local Refine protocol in cryoSPARC to obtain the final map. The final resolution reported in the manuscript was calculated in cryoSPARC at FSC=0.143 for all maps.

F_{ECTO} [FIP-HRC]$_2$-PEG$_{11}$

The F_{ECTO}-[FIP-HRC]$_2$-PEG$_{11}$ structure was recorded and processed following the same workflow as the F_{ECTO}-Fab 77 structure. The number of particles and workflow overview is presented in **Fig. S5B**.

F_{ECTO}

The F_{ECTO} dataset was acquired as described above, with minor modifications. An increased electron exposure of 70 e-/Å² was used for data acquisition. Initial data processing was conducted in cryoSPARC version 4.3 Live, where 4.6M particles were extracted from 7,980 micrographs through blob picking. A deep

2D classification protocol in cryoSPARC was applied to these particles, from which the best candidates were selected for training of the Topaz model. After Topaz extraction, 12M particles were extracted at a box size of 420 px and Fourier-cropped to 64 px.

Through intensive deep 2D classification, a final dataset comprising 1.7M particles of high quality was obtained. These particles were then subjected to an initial 3D reconstruction to recenter 3D coordinates, after which they were re-extracted at a box size of 420 px and Fourier-cropped to 300 px. A 3D reconstruction from Homogeneous refinement yielded a resolution of 2.19 Å in C3 symmetry. After symmetry expansion to C3, the particles were classified into 10 distinct classes through 3D classification in cryoSPARC, with a high-resolution limit set at 2.0 Å. The class with the highest resolution, 2.11 Å, was selected for further processing. Local and global CTF refinements were performed, and the final refinement was done using a local refinement protocol. Detailed processing is shown in Fig S5 A.

Post-fusion F_{ECTO}

F_{ECTO} was incubated in lower salt buffer (50 mM HEPES pH 8.0, 150 mM NaCl) for 1 week at 4°C. Quantifoil R1.2/1.3 grids were used to freeze F_{ECTO} in post-fusion confirmation. F_{ECTO} (3 µL of 0.5 mg/ml) was mixed with 1 µL 0.36 mM Lauryl Maltose Neopentyl Glycol (LMNG), blotted for 6 s, and frozen in liquid ethane. The data processing was similar to the F_{ECTO}-Fab 77 dataset. For the post-fusion conformation, data processing involved selecting particles based on size and shape, specifically top views of approximately 70 Å in diameter and extended side views. The detailed processing is illustrated in Figure S5 D.

Fab 77-stabilized F_{ECTO} fragment and refolding intermediates

To determine the structure of the F_{ECTO} fragment stabilized by Fab 77, we reprocessed the F_{ECTO}-Fab 77 dataset in cryoSPARC 4.4. Corrected movies were imported, and Patch CTF was used to estimate the contrast transfer function values. A permissive blob picker (80-120 Å, 0.2 minimum separation distance) yielded 5.6M particles, which underwent Deep2D classification. Classes corresponding to F_{ECTO}-Fab 77 and unresolved junk classes were rejected, and the remaining particles were used for multiple rounds of Deep2D classification. Finally, 17,000 particles showing intermediate states of refolding were used to train the Topaz model. After extraction, particles were divided into those containing the Fab 77-stabilized F_{ECTO} fragment and intermediate refolding steps. For refolding intermediates, ~35,000 particles were selected, and ~700 corresponded to the intermediate refolding step, ~2,000 to the protomer-separated state, and ~230,000 to the Fab 77-stabilized F_{ECTO} fragment. The latter were re-extracted at 340 px, and Fourier cropped to 160 px. Extracted particles were again subjected to Deep2D classification using a high-resolution information cutoff at 3 Å. Only the best-looking classes were selected (94,000), and the initial model was calculated with high-resolution information up to 3 Å. Homogeneous, non-homogeneous, and local refinements were used to calculate the final map, including the whole Fab fragment. The map region corresponding to the constant region of the Fab was removed in ChimeraX, and a soft binary mask was calculated using Relion. The final map was calculated using the local refinement procedure with a focused mask centered on the Fab 77-F_{ECTO} fragment interface by adjusting the fulcrum coordinates.

Model building

For the F_{ECTO}-Fab 77 structure, the obtained cryo-EM map was used to dock the previously published F X-ray structure (PDB ID: 5XYW (*52*)) using ChimeraX. Next, the antibody model was generated with an in-house implementation of ColabFold based on AlphaFold2 (*100*, *101*). Once the models were positioned, manual model building was conducted in Coot 0.9.8.7, sourced from the CCP4 package (*102*, *103*). An automatically sharpened and density-modified map from PHENIX ResolveEM (using only half-maps) was the basis for model building (*104*). A real-space refinement protocol followed manual model building in the PHENIX package, consisting of 10 macrocycles without any enforced restraints, and increased the number of Max iterations to 800 (*105*). Finally, water placement was carried out manually on a density-modified map. Water molecules were positioned where spherical density was visible at map RMSD > 5.0, no more than 2.7 Å from protein atoms. Interfaces were analyzed using ChimeraX and PISA server (*106*). Electrostatic maps, as well as the generation of F variants, were calculated in ChimeraX. Local map scales for F_{ECTO} were calculated in OccuPy (*107*).

F_{ECTO} in the post-fusion conformation was first generated using homology modeling using SWISS-MODEL software and manually rebuilt in Coot(*108*). Refinement and evaluation of the model was done as described above.

In the case of the F_{ECTO} fragment stabilized by Fab 77, the structure of F_{ECTO}-Fab 77 was fitted into the obtained map. Residues located within this map were retained, and portions of the model not encompassed by the map were removed. Subsequently, the remaining model underwent relaxation with Isolde (*109*), manual Coot adjustments, and PHENIX refinement.

Heat-Induced refolding of F_{ECTO}-Fab 77

A 7.5 µM solution of F_{ECTO} in HBS containing 800 mM NaCl was combined with a 1.5-fold molar excess of Fab 77. This mixture was then diluted four-fold using 50 mM HEPES (pH 8.0), resulting in a final NaCl concentration of approximately 150 mM. The complex was allowed to form at room temperature over 4 hrs. A 15 µL aliquot of the formed complex was transferred to a PCR tube and subjected to heat treatment in a PCR thermocycler. The incubation times tested were 1, 5, 7.5, or 10 min at 50 ℃ and 1 or 5 min at 55℃. After incubation, the samples were rapidly cooled by placing the tube on ice for 5 min. Negative stain grids were then prepared using the described protocol.

The acquired data were processed using cryoSPARC 4.3. After motion correction and estimation of CTF values, particle picking was performed using the blob picker. Subsequent 2D classification was performed using the previously described deep 2D classification protocol to separate particles into distinct classes.

Sequence analysis

Approximately 1400 MeV genomic sequences were obtained from the nucleotide NCBI database. CDS regions were manually annotated and curated to include only those between 400 and 600 amino acid residues in length with pairwise alignment scores greater than zero as compared to the F WT sequence (Uniprot: Q786F3). The resulting ~820 sequences were aligned using Clustal Omega, and the conservation score was computed using AL2CO(*89*). Conservation scores were placed on the 3D models of F_{ECTO}^{PRE} and F_{ECTO}^{POST} in ChimeraX using AL2CO. Sequence variants were determined using a Python script based on the multiple sequence alignment file.

Glycoproteomics sample preparation

For glycoproteomics analysis, a SP3 sample preparation protocol was applied (*110*) . Recombinant measles F_{ECTO} was denatured in the buffer with 2% SDS, 200 mM Tris/HCl, 10 mM tris(2-carboxyethyl)phosphine, pH 8.0, at 95 °C for 10 min followed with 30 min reduction at 37 °C for 30 min. Samples were next alkylated by adding 40 mM iodoacetamide and incubated in the dark at room temperature for 45 min. 3 µg recombinant F_{ECTO} was used for each protease digestion. Samples were split in half for parallel digestion with chymotrypsin (Sigma) and alpha lytic protease (Sigma). Sera-Mag beads (GE Healthcare) were used at a bead/protein ratio of 10:1 (wt/wt) for protein binding. Ethanol was added to the protein-beads mixture reaching final concentration 80% to enhance binding. The mixture was incubated at RT for 10 min at 1000 r.p.m. in a ThermoMixer. The supernatant was removed and protein-bound-beads washed three times with 80% ethanol. Measles F_{ECTO} was digested on beads overnight at 37 °C in 25 µL 50 mM ammonium bicarbonate at 1000 r.p.m in a ThermoMixer. The supernatant was taken for MS analysis.

Glycoproteomics LC-MS/MS measurements

The experiments were performed as previously described (*111*) with minor modifications, as follows. For each sample and protease digestion, approximately 50 ng of peptides were run by online reversed phase chromatography on an Dionex UltiMate 3000 (Thermo Fisher Scientific) coupled to a Thermo Scientific Orbitrap Fusion mass spectrometer. A Poroshell 120 EC C18 (50 cm × 75 µm, 2.7 µm, Agilent Technologies) analytical column and a ReproSil-Pur C18 (2 cm × 100 µm, 3 µm, Dr. Maisch) trap column were used for peptide separation. Duplicate samples were analyzed with two different mass spectrometry methods, using identical LC-MS parameters and distinct fragmentation schemes. In one method, peptides were subjected to Electron Transfer/Higher-Energy Collision Dissociation (HCD) fragmentation. In the other method, all precursors were subjected to HCD fragmentation, with additional EThcD fragmentation triggered by the presence of glycan reporter oxonium ions. A 90 min LC gradient from 0% to 44% acetonitrile was used to separate peptides at a flow rate of 300 nl/min. Data was acquired in data-dependent mode. Orbitrap Fusion parameters for the full scan MS spectra were as follows: a standard AGC target at 60 000 resolution, scan range 350–2000 m/z, Orbitrap maximum injection time 50 ms. The ten most intense ions (2+ to 8+ ions) were subjected to fragmentation. For the EThcD fragmentation scheme, the supplemental higher energy collision dissociation energy was set at 27%. MS2 spectra were acquired at a resolution of 30,000 with an AGC target of 800%, maximum injection time 250 ms, scan range 120–4000 m/z and dynamic exclusion of 16 s. For the triggered HCD-EThcD method, the LC gradient and MS1 scan parameters were identical. The ten most intense ions (2+ to 8+) were subjected to HCD fragmentation with 30% normalized collision energy from 120–4000 m/z at 30,000 resolution with an AGC target of 100% and a dynamic exclusion window of 16 s. Scans containing any of the following oxonium ions within 20 ppm were followed up with additional EThcD fragmentation with 27% supplemental HCD fragmentation. The triggering reporter ions were: Hex(1) (129.039; 145.0495; 163.0601), PHex(1) (243.0264; 405.0793), HexNAc(1) (138.055; 168.0655; 186.0761), Neu5Ac(1) (274.0921; 292.1027), Hex(1)HexNAc(1) (366.1395), HexNAc(2) (407.166), dHex(1)Hex(1)HexNAc(1) (512.1974), and Hex(1)HexNAc(1)Neu5Ac(1) (657.2349). EThcD spectra were acquired at a resolution of 30,000 with a normalized AGC target of 400%, maximum injection time 250 ms, and scan range 120–4000 m/z.

Glycoproteomics data analysis

The acquired data was analysed using Byonic (v4.5.2) against a custom database of recombinant F_{ECTO} and the proteases used in the experiment, searching for glycan modifications with 12/24 ppm search windows for MS1/MS2, respectively. Up to ten missed cleavages were permitted using C-terminal cleavage at F/Y/W/M/L for chymotrypsin, or T/A/S/V for alpha lytic protease. For N-linked analysis, carbamidomethylation of cysteine was set as fixed modification, oxidation of methionine/tryptophan as variable common 1, and hexose on tryptophan as variable rare 1. N-glycan modifications were set as variable common 2, allowing up to max. 2 variable common and 1 rare modification per peptide. All N-linked glycan databases from Byonic were merged into a single non-redundant list to be included in the database search. All reported glycopeptides in the Byonic result files were manually inspected for quality of fragment assignments (with scores ≥ 200). All glycopeptide identifications from both EThcD and HCDpdEThcD runs were merged into a single non-redundant list per sequon. Glycans were classified based on HexNAc content as truncated (≤ 2 HexNAc; < 3 Hex), paucimannose (2 HexNAc, 3 Hex), oligomannose (2 HexNAc; > 3 Hex), hybrid (3 HexNAc) or complex (> 3 HexNAc). Byonic search results were exported to mzIdentML format to build a spectral library in Skyline (v22.2.0.312) and extract peak areas for individual glycoforms from MS1 scans. The full database of variable N-linked glycan modifications from Byonic was manually added to the Skyline project file in XML format. Reported peak areas were pooled based on the number of HexNAc, Fuc or NeuAc residues to distinguish truncated, paucimannose, oligomannose, hybrid, and complex glycosylation, or the degree of fucosylation and sialylation, respectively.

Statistical analysis

All data analysis and visualizations were conducted using a Python notebook integrating SciPy, Matplotlib, Pandas, Seaborn, and Statannotations packages (*112–114*). Statistical significance was determined using the Mann-Whitney test. For p-value annotations, the following symbols were used: 'ns' indicates p <= 1,* represents 0.01 < p <= 0.05,** signifies 0.001 < p <= 0.01, and *** stands for 0.0001 < p <= 0.001.

Chemicals and peptides

Chemicals and peptides used here were previously described in (*53*). The description is reported here with minimal modification. *N*-(3-cyanophenyl)-2-phenylacetamide (also known as 3G) was commercially acquired from ZereneX Molecular Limited (UK).

Peptides were purchased from CPC, Ltd. Bromoacetyl cholesterol and bismaleimide cholesterol derivatives were custom-made by Charnwood Molecular Ltd. Dimethylsulfoxide (DMSO), tetrahydrofuran (THF) and *N,N*-diisopropylethylamine (DIPEA) were purchased from Sigma Aldrich, and bismaleimide-PEG_{11} was from Quanta BioDesign. HPLC purification was performed on an 1100 Series Agilent HPLC system equipped with a UV diode array detector and a fraction collector using a reverse phase (RP.) Phenomenex Jupiter C4 LC column 300Å (150 x 21.2 mm, particle size 5 µm). MALDI-TOF analysis was performed on Bruker ultrafleXtreme MALDI-TOF-TOF instrument.

Acknowledgments

We thank J. S. Orange for his support. We thank Michael Norris for valuable discussions at project outset, and Theresa Gewering and Haoyang Li for assisting with the model evaluation. We thank Tiziana F. Bovier

for technical assistance in viral rescue. We thank Marissa Acciani and Sharon Schendel for careful reading of the manuscript and suggestions. We thank the cryo-EM facility of La Jolla Institute for Immunology for assistance with data collection and acknowledge the GHR Foundation and private donors for support of instrumentation.

Funding: This work was supported by the National Institutes of Health (NS105699, NS091263, and AI176833) to MP, Swiss National Science Foundation Postdoc Mobility fellowships P2EZP3_195680 (DSZ) and P500PB_210992 (DSZ), Measles Virus Biobank (https://ciri.ens-lyon.fr/teams/IbIV/measles-biobank), the Dutch Research Council NWO Gravitation 2013 BOO, Institute for Chemical Immunology ICI 024.002.009 (to JS), and institutional funds of La Jolla Institute for Immunology (EOS).

Author contributions:

DSZ: Designed protein constructs, cloned and expressed proteins, designed and performed DSF and DLS experiments, expressed and digested antibodies, recorded all negative stain and cryo-EM data, processed and solved structures, performed the point mutation analysis, wrote the code for analysis, analyzed all data present in the manuscript, prepared figures, and wrote the manuscript, RDM: Virological and cell biology experimentation, data analysis, GN: Assisted with the F_{ECTO}-Fab complex screening, protein purification, NS-EM, and DSF, GZ: Cell biology experimentation, and data analysis, KS: Data analysis, CL: In vivo experimentation and data analysis, EBS: Viral sequencing and data interpretation, HMC: Assisted with initial protein expression optimization and kinetic analysis, CH: Measured Biolayer interferometry for FECTO and Fab, WP: Glycoproteomics analysis and interpretation, DP: Assisted with cloning, expression, and purification of constructs, TCM: Assisted data curation and analysis, RDA: Assisted with the cryo-EM data acquisition and maintained microscopes, BH: Reagents and result interpretation, CM: Virological support and result interpretation, JS: Glycoproteomics analysis and interpretation, funding, ALG: Supervised viral sequencing and data interpretation, KMH: Data analysis, kinetic measurements, manuscript writing, and figure preparation, SN: In vivo experimentation, data analysis and interpretation, supervision, manuscript writing, AM: Results analysis and interpretation, supervision, manuscript writing, MP: Designed proteins and antibodies, virological experimentation, cell biological experimentation, results analysis and interpretation, supervision, funding, manuscript writing, EOS: Results analysis and interpretation, supervision, funding, manuscript writing.

Competing interests:

Colombia University has filed a provisional patent related to the 77 antibody [US 18/491,733, continuation-in-part of PCT/US22/25619 (expired) which claimed priority to US 63/177,224 (expired)]. The inventors are Matteo Porotto, Anne Moscona, Branka Horvat, and Cyrille Mathieu. The other authors declare that they have no competing interests in relation to the work described in this manuscript.

Data availability

Structural models are deposited in the protein data bank (PDB, https://www.rcsb.org/).The PDB IDs are: F_{ECTO}: 8UUP, F_{ECTO}-FIP-HRC: 8UUQ, F_{ECTO}-Fab77: 8UT2, F_{ECTO} post-fusion: 8UTF, Fab 77-stabilized F_{ECTO} fragment: 9AT8. Cryo-EM maps are deposited in the EM Database (https://www.emdataresource.org/) with the following IDs: FECTO: EMD-42593, F_{ECTO}-FIP-HRC: EMD-42595, F_{ECTO}-Fab77: EMD-42527,

928 F_{ECTO} post-fusion: EMD-42539, Fab 77-stabilized F_{ECTO} fragment (masked): EMD-43827, Fab 77-stabilized F_{ECTO} fragment: EMD-43828. The raw LC-MS/MS files and glycopeptide identifications have been
930 deposited to the ProteomeXchange Consortium via the PRIDE partner repository with the dataset identifier PXD050366. Post-publication, all research materials referenced in this study will be made available upon
932 reasonable request through Material Transfer Agreements (MTAs).

934

Supplementary material:

936 Figs. S1 to S12

Tables S1 to S5

938 Movie S1

References 1-116

940 MDAR Reproducibility Checklist

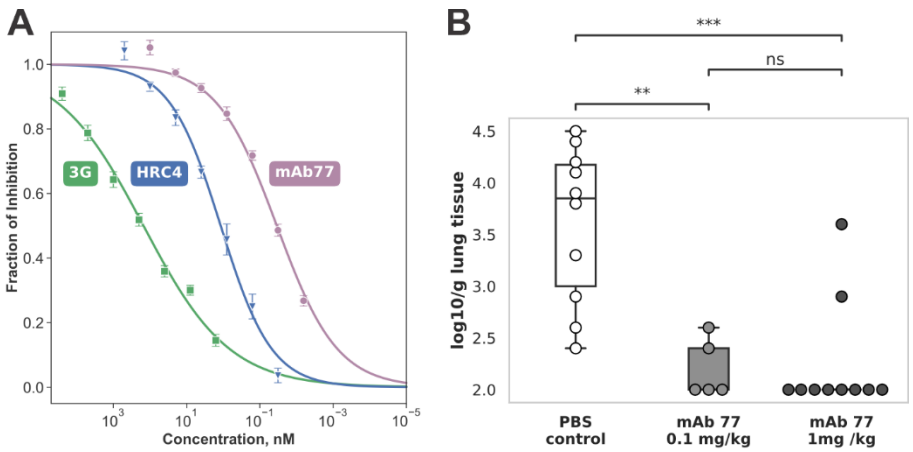

Figure 1. mAb 77 displays robust antiviral activity in vitro and in vivo.

A) Antiviral potency of mAb 77 (violet) in a viral entry assay to measure inhibition of infection in Vero cells expressing SLAM/CD150. The activity was compared to established MeV inhibitors, 3G (green; (*51*)) and HRC4 (blue; (*53*)). Values for IC_{50} and Hill slope were estimated using logistic regression. 3G: IC_{50}=150.1±16.2 nM, Hills slope=0.37±0.01, HRC4: IC_{50}=1.17±0.27 nM, Hills slope=0.62±0.07, mAb 77: IC_{50}=0.034±0.005 nM, Hills slope=0.52±0.04. Each point with an error bar shows the average of three separate biological tests, ± the standard error. B) Antibody transfer experiment to assess *in vivo* protective efficacy of mAb 77. Cotton rats received intraperitoneal (IP) injections of 0.1 mg/kg or 1 mg/kg mAb 77 12 hours before challenge with MeV. Animals in the control group received PBS before the challenge. Values correspond to MeV titers in lung tissue collected four days post-infection. The line inside the box represents the median value. Significance was shown using the Mann-Whitney-Wilcoxon test. P-value annotation legend: ns (non-significant): p <= 1.00, *: 0.01 < p <= 0.05, **: 0.001 < p <= 0.01, ***: 0.0001 < p <= 0.001.

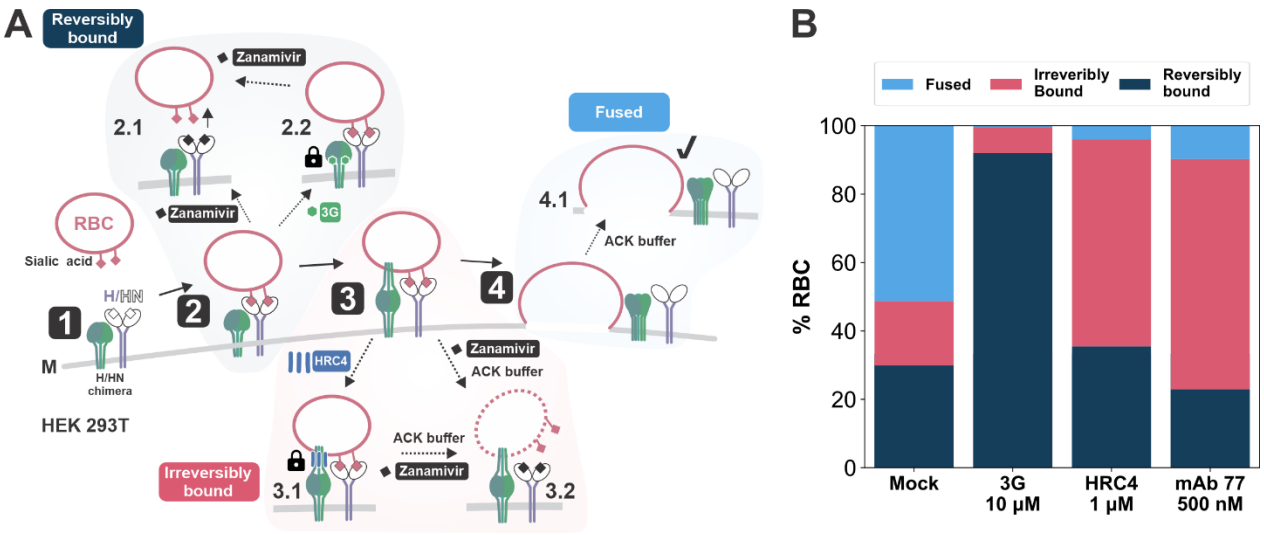

Figure 2. mAb 77 mirrors the action of the HRC4 inhibitor and stabilizes the extended state of F protein.

(A) Schematic representation of the red blood cell (RBC) fusion assay conducted in HEK 293T cells expressing a chimeric HN-H receptor binding protein with MeV F protein. (1) Without fusion inhibitors, the HN-H binds sialic acid on the RBCs. The MeV H stalk region subsequently activates the F protein, facilitating its refolding to a fusion intermediate that anchors the fusion peptide in the RBC membrane, culminating in the fusion of RBC and HEK 293T membranes. (2) In the presence of Zanamivir, a small-molecule inhibitor that competitively binds the HN sialic acid receptor binding site, reversible binding of RBCs to HN is observed (2.1). Adding 3G locks the F protein in its pre-fusion conformation, resulting in only reversible binding of most RBCs to the HN-H (2.2). (3) The subsequent checkpoint is evaluated through combined administration of Zanamivir and ACK buffer. Zanamivir acts as described in (2), whereas ACK buffer induces lysis of RBCs (dashed line). At this checkpoint, fusion intermediates with anchored fusion peptides within RBC membranes, such as those stabilized by HRC4, resist Zanamivir-induced dissociation (left, 3.1) but are lysed in the presence of ACK buffer (right, 3.2). (4) At the last checkpoint, complete fusion of RBC and HEK 293T membranes is achieved. Here, ACK buffer addition has no impact on the fused RBCs (4.1). (B) Bar chart summarizing the results of a mechanistic assay comparing various known inhibitors and mAb 77. For each condition, cells were categorized based on their interaction with red blood cells (RBCs): reversibly bound (dark blue) in which RBCs were adhered only by chimeric H and could be removed by treatment with Zanamivir; irreversibly bound (pink) in which RBCs were initially attached by chimeric H, but subsequent F protein refolding anchored the fusion peptide in the RBC membrane, making RBC attachment insensitive to Zanamivir with RBC retained on the HEK 293T cell surface; and fused (light blue) in which RBCs underwent membrane fusion with HEK 293T cells expressing the fusion complex.

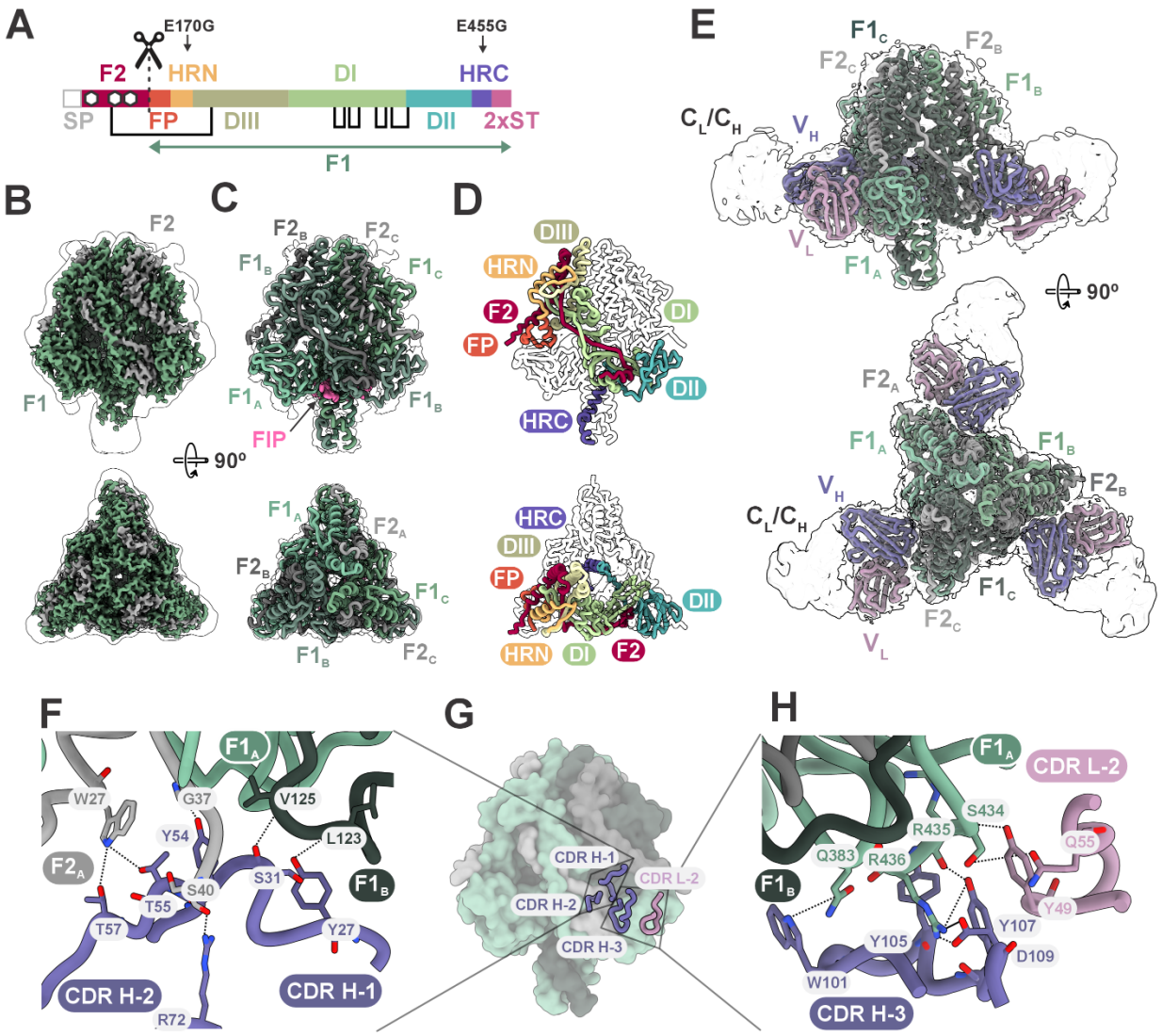

Figure 3. Cryo-EM structure of mAb 77 Fab fragment engaging F_{ECTO} at the base of the head domain.

A) Primary structure annotation of F_{ECTO}. Functional domains are delineated as color-coded rectangular regions: SP, Signal Peptide; FP, Fusion Peptide; HRN, N-terminal Heptad Repeat; DIII, Domain III; DI, Domain I; DII, Domain II; HRC, C-terminal Heptad Repeat; 2xST, Twin Strep-Tag II. White hexagons denote glycosylation sites within the F2 region. A black loop represents natural disulfide bonds. Black scissors indicate the furin cleavage site that divides the precursor F0 into F2 and F1 subunits. Arrows indicate the locations of two stabilizing mutations. B) A 2.1-Å resolution map of F_{ECTO}, showing F1 (green) and F2 (gray) with low-resolution map overlay showing details included in the map (silhouette). C) Ribbon representation of the 2.3-Å resolution structure of F_{ECTO} in the presence of fusion inhibitor peptide (FIP)with a low resolution map as a silhouette. D) Domain description of F_{ECTO}, colored from N terminus to C terminus (red to purple), as in A). E) A ribbon representation of F_{ECTO} in complex with three copies of Fab 77. The Fabs interact symmetrically with the lower section of the head domain in a cleft between domains I and II. The F_{ECTO} F1 chain is represented in green, the F2 chain in gray, the 77 Fab heavy variable domain (VH) in violet, and the light variable domain (VL) in pale pink. The cryo-EM map, delineated as a silhouette, also encompasses the masked-out region, including the constant light and heavy segments (CL and CH) of the

Fab 77. F) CDR loops H1 and H2 of Fab 77 establish hydrogen bonds with three distinct F_{ECTO} polypeptide chains: $F2_A$ (light gray), $F1_A$ (light green), and $F1_B$ (dark green). The interacting residues on F_{ECTO} and Fab 77 are shown in the respective colors of their chains. Interface residues F1B 383, 384, and CRD-H1 32, 33 are omitted for better visibility. Dashed lines depict the selected hydrogen bonds. G) The VH region of Fab 77 contributes the majority of interactions with F, and all three heavy chain complementarity-determining regions (CDRs H1, H2, and H3) engage with the head domain. Only one CDR L2 from the VL domain contributes to the interaction. Black rectangles show regions enlarged in F) and H). H) The CDR H3 and L2 interact with only a single F_{ECTO} chain, $F1_A$. The interacting residues are highlighted in the color of the respective chains as in E). Dashed lines represent chosen hydrogen bonds; a solid line indicates a salt bridge.

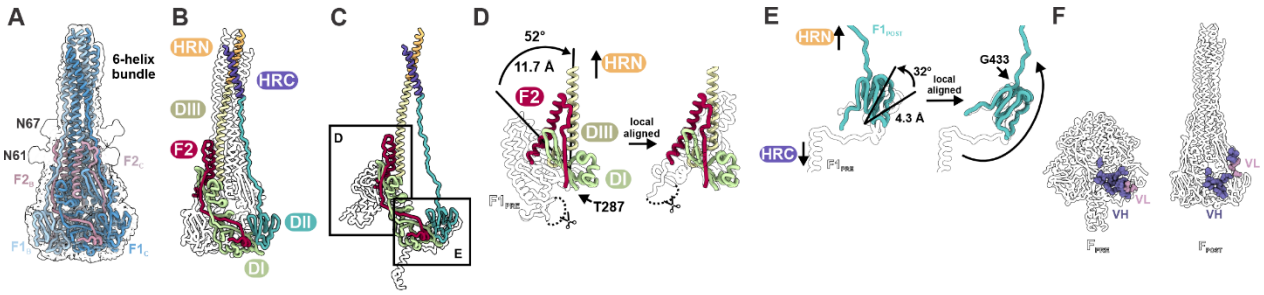

Figure 4. The post-fusion conformation of F_{ECTO} shows significant structural domain reconfiguration that facilitates membrane fusion.

A) Cryo-EM structure of F_{ECTO} in its post-fusion conformation revealing a structural rearrangement of the HRN and HRC, forming a canonical post-fusion 6-helix bundle. F1 and F2 are in shades of blue and pink, respectively. The cryo-EM map is displayed as a silhouette, with two notable glycosylation sites (N61 and N67) indicated and visualized only at the map level. B) Domain-based coloring of F_{ECTO} in the post-fusion conformation as in Fig. 3D. C) Global alignment comparison between F_{ECTO} in pre-fusion (depicted in white with silhouette) and post-fusion (in domain color scheme) conformations. Optimal global alignment per chain was attained by aligning F_{ECTO} on domain I (highlighted in light green). Regions that undergo significant conformational changes are surrounded in boxes and shown in panels D and E. D) Domain III undergoes the most dramatic shift between pre- and post-fusion, moving its center of mass over by 11 Å and rotating by 52°. Most of the fold remains unchanged when local alignment is performed on the sequence region corresponding to the domain region, with the most notable changes seen in the HRN, which releases the fusion peptide and refolds from multiple disjoined α-helices and β-strands into an ~100 Å extended helix. The furin-containing loop is depicted as a dashed line. Scissors symbolize the furin cleavage site. E) Domain II undergoes a twisting motion during the refolding step. Only slight differences are observed in the fold after local alignment for the residue range corresponding to the domain. The C-terminal region of the domain undergoes the most significant change. The HRC changes direction by nearly 180° around residue G433. HRC in black and color corresponds to the pre-fusion and post-fusion structure, respectively. F) Mapping of residues comprising the mAb 77 epitope on both the pre- and post-fusion states of F_{ECTO} reveals displacement of the epitope in the post-fusion state that explains the lack of mAb 77 binding to F_{ECTO} in the post-fusion conformation.

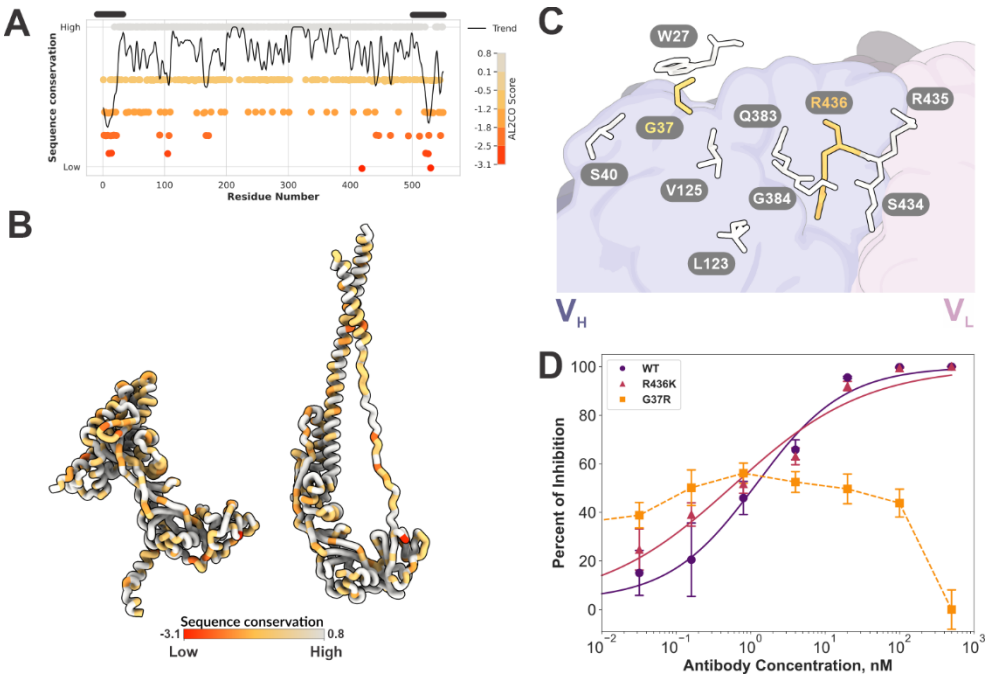

Figure 5. Structural analysis of MeV F sequence conservation and viral evolution assay reveals consistent conservation across the protein.

A) Conservation map of the MeV F full-length (FL) primary sequence derived from over 830 F sequences in the NCBI protein database. The sequences were aligned using Clustal Omega(*88*), and the AL2CO algorithm(*89*) was used to calculate the conservation score. MeV F demonstrates uniform sequence conservation, with only two regions having lower conservation: the signal peptide and the cytoplasmic tail, which are highlighted by black lines at the top of the plot. B) Mapping the AL2CO score onto the tertiary pre- and post-fusion structure of F_{ECTO} shows no conservation hotspots. In general, less exposed residues show higher sequence conservation compared to solvent-exposed residues. C) Most residues forming the mAb 77 epitope demonstrate high sequence conservation (light gray), but G37 and R437 (shown in shades of yellow) have been found in natural variants. D) Cell-based fusion inhibition assay to examine the impact of G37R and R436K mutations on mAb 77 binding affinity. The R436K mutation is common but has minimal influence on inhibition of antibody-mediated fusion. Conversely, the rarer G37R mutation could evade fusion inhibition by mAb 77.

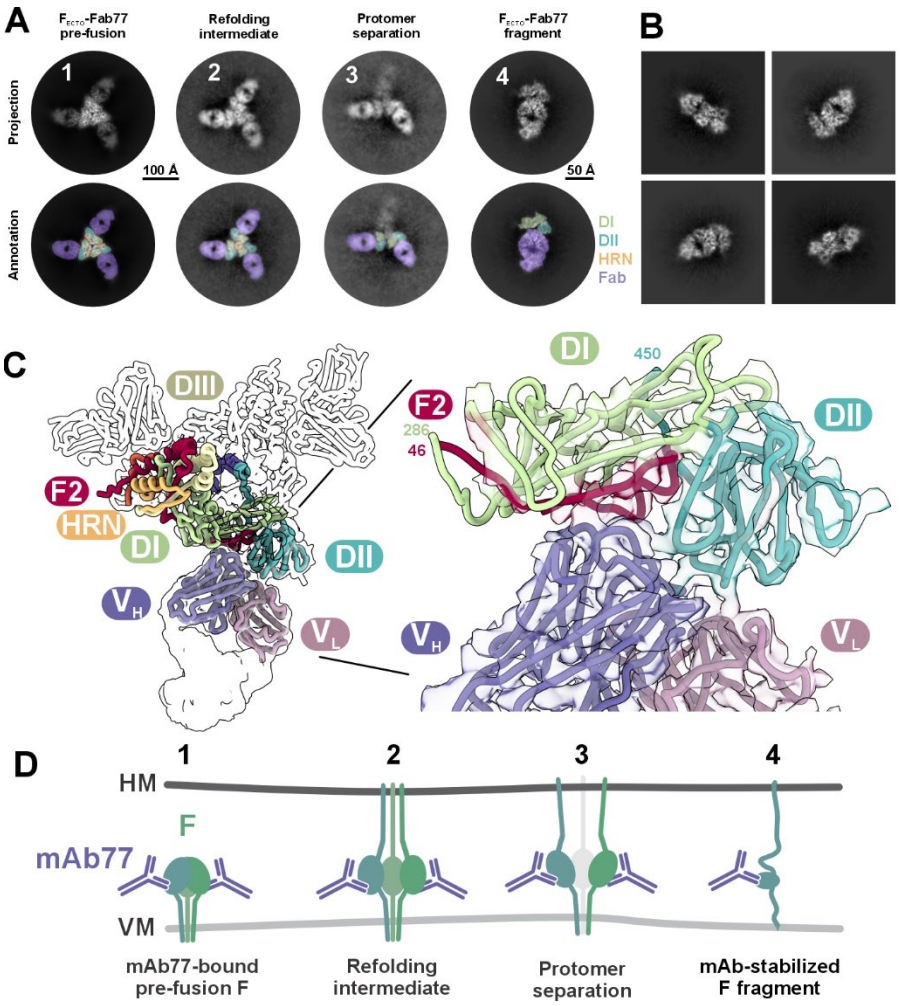

Figure 6. Cryo-EM to elucidate mAb 77 mechanism of action.

A) 2D classes show conformational heterogeneity in the F_{ECTO}-Fab77 dataset. Using an extensive 2D classification procedure, we could isolate 2D classes that constituted less than 1% of the dataset. The leftmost panel, Panel 1, shows a 2D projection of the final volume of F_{ECTO}-Fab77, followed by classes that depict intermediate refolding steps during Fab77-induced F_{ECTO} refolding. Panel 2 shows a refolding intermediate, clearly showing a missing density corresponding to the HRN domain and a lack of density between Fab77-bound domain II (DII, cyan) and domain I (DI, light green) of neighboring protomers. Panel 3 shos a conformational state with protomer separation, which finally leads to a stabilized F fragment (domains I and II) by Fab77 in Panel 4. The upper and lower circles correspond to the projection and annotation based on the projection, respectively. Colors correspond to the domains: purple Fab77, light green domain I, dark green domain II, and orange HRN. Scale bars correspond to 100 Å (first three classes) and 50 Å (last class). F2 was omitted from the annotated image for clarity.

B) Cryo-EM 2D class averages of Fab 77 stabilizing a fragment of F_{ECTO}.

C) Approximately 3.6 Å resolution density map of the Fab 77-F_{ECTO} fragment superimposed on the trimeric F_{ECTO}-Fab 77 complex. A zoomed-in view of the corresponding density associated with only a stabilized portion of F_{ECTO} is shown on the right. The interaction between Fab 77 and F_{ECTO} maintains stabilization of the previously characterized epitope to inhibit further refolding. Domain coloring follows the scheme presented in Figure 3. The left map was Gaussian blurred to 1.5 standard deviations to simplify visualization. Residues corresponding to the F_{ECTO} fragment are indicated.

D) The proposed mechanism of action for mAb 77 depicts the observed populations of F_{ECTO}-Fab 77 complexes across the reported experiments. Numbers for each stage of refolding correspond to those in panel A.

References and notes

1. S. L. Katz, A. R. Hinman, Summary and conclusions: measles elimination meeting, 16-17 March 2000. *J. Infect. Dis.* **189 Suppl 1**, S43-7 (2004).

2. A. P. Fiebelkorn, S. B. Redd, P. A. Gastañaduy, N. Clemmons, P. A. Rota, J. S. Rota, W. J. Bellini, G. S. Wallace, A comparison of postelimination measles epidemiology in the United States, 2009-2014 versus 2001-2008. *J. Pediatric Infect. Dis. Soc.* **6**, 40–48 (2017).

3. P. A. Gastañaduy, S. B. Redd, A. P. Fiebelkorn, J. S. Rota, P. A. Rota, W. J. Bellini, J. F. Seward, G. S. Wallace, Measles—United States, January 1–May 23, 2014. *Am. J. Transplant* **14**, 1937–1940 (2014).

4. M.-M. A. Fill, D. Sweat, H. Morrow, A. Haushalter, J. C. Martin, T. Zerwekh, T. Chakraverty, J. Kmet, K. Morris, K. Moore, M. Kainer, R. Murphree, J. R. Dunn, W. Schaffner, T. F. Jones, Notes from the Field: Measles Outbreak of Unknown Source - Shelby County, Tennessee, April-May 2016. *MMWR Morb. Mortal. Wkly. Rep.* **65**, 1039–1040 (2016).

5. W. Orenstein, K. Seib, Mounting a good offense against measles. *N. Engl. J. Med.* **371**, 1661–1663 (2014).

6. V. K. Phadke, R. A. Bednarczyk, D. A. Salmon, S. B. Omer, Association Between Vaccine Refusal and Vaccine-Preventable Diseases in the United States: A Review of Measles and Pertussis. *JAMA* **315**, 1149–1158 (2016).

7. Nearly 40 million children are dangerously susceptible to growing measles threat, *CDC* (2022). https://www.cdc.gov/media/releases/2022/p1123-measles-threat.html.

8. A 30-fold rise of measles cases in 2023 in the WHO European Region warrants urgent action. https://www.who.int/europe/news/item/14-12-2023-a-30-fold-rise-of-measles-cases-in-2023-in-the-who-european-region-warrants-urgent-action.

9. K. Bochennek, R. Allwinn, R. Langer, M. Becker, O. T. Keppler, T. Klingebiel, T. Lehrnbecher, Differential loss of humoral immunity against measles, mumps, rubella and varicella-zoster virus in children treated for cancer. *Vaccine* **32**, 3357–3361 (2014).

10. C. I. Paules, H. D. Marston, A. S. Fauci, Measles in 2019 - Going Backward. *N. Engl. J. Med.* **380**, 2185–2187 (2019).

11. A. Fox, T. M. Hung, H. Wertheim, L. N. M. Hoa, A. Vincent, B. Lang, P. Waters, N. H. Ha, N. V. Trung, J. Farrar, N. Van Kinh, P. Horby, Acute measles encephalitis in partially vaccinated adults. *PLoS One* **8**, e71671 (2013).

12. G. A. Poland, R. M. Jacobson, The re-emergence of measles in developed countries: time to develop the next-generation measles vaccines? *Vaccine* **30**, 103–104 (2012).

13. J. A. Whitaker, T. D. Shanafelt, G. A. Poland, N. E. Kay, Room for improvement: immunizations for patients with monoclonal B-cell lymphocytosis or chronic lymphocytic leukemia. *Clin. Adv. Hematol. Oncol.* **12**, 440–450 (2014).

14. A. Schuchat, A. P. Fiebelkorn, W. Bellini, Measles in the United States since the Millennium: Perils and Progress in the Postelimination Era. *Microbiol Spectr* **4** (2016).

15. S. Bhattacharyya, M. J. Ferrari, Age-specific mixing generates transient outbreak risk following critical-level vaccination. *Epidemiol. Infect.* **145**, 12–22 (2017).

16. M. S. Gallone, C. Germinario, A. Larocca, S. Tafuri, Long time immunogenicity of measles vaccine in the vaccination era: An open question. *Hum. Vaccin. Immunother.* **13**, 117–119 (2017).

17. S. B. Sowers, J. S. Rota, C. J. Hickman, S. Mercader, S. Redd, R. J. McNall, N. Williams, M. McGrew, M. L. Walls, P. A. Rota, W. J. Bellini, High Concentrations of Measles Neutralizing Antibodies and High-Avidity Measles IgG Accurately Identify Measles Reinfection Cases. *Clin. Vaccine Immunol.* **23**, 707–716 (2016).

18. R. Seither, O. B. Yusuf, D. Dramann, K. Calhoun, A. Mugerwa-Kasujja, C. L. Knighton, Coverage with selected vaccines and exemption from school vaccine requirements among children in kindergarten — United States, 2022–23 school year. *MMWR Morb. Mortal. Wkly. Rep.* **72**, 1217–1224 (2023).

19. J. F. Seward, W. A. Orenstein, Editorial commentary: A rare event: a measles outbreak in a population with high 2-dose measles vaccine coverage, *Clinical infectious diseases: an official publication of the Infectious Diseases Society of America*. **55** (2012)pp. 403–405.

20. G. De Serres, N. Boulianne, F. Defay, N. Brousseau, M. Benoît, S. Lacoursière, F. Guillemette, J. Soto, M. Ouakki, B. J. Ward, D. M. Skowronski, Higher risk of measles when the first dose of a 2-dose schedule of measles vaccine is given at 12-14 months versus 15 months of age. *Clin. Infect. Dis.* **55**, 394–402 (2012).

21. I. H. Haralambieva, I. G. Ovsyannikova, M. O'Byrne, V. S. Pankratz, R. M. Jacobson, G. A. Poland, A large observational study to concurrently assess persistence of measles specific B-cell and T-cell immunity in individuals following two doses of MMR vaccine. *Vaccine* **29**, 4485–4491 (2011).

22. C.-J. Chen, P.-I. Lee, Y.-C. Hsieh, P.-Y. Chen, Y.-H. Ho, C.-J. Chang, D.-P. Liu, F.-Y. Chang, C.-H. Chiu, Y.-C. Huang, C.-Y. Lee, T.-Y. Lin, Waning population immunity to measles in Taiwan. *Vaccine* **30**, 6721–6727 (2012).

23. M. Kontio, S. Jokinen, M. Paunio, H. Peltola, I. Davidkin, Waning antibody levels and avidity: implications for MMR vaccine-induced protection. *J. Infect. Dis.* **206**, 1542–1548 (2012).

24. I. H. Haralambieva, R. B. Kennedy, I. G. Ovsyannikova, J. A. Whitaker, G. A. Poland, Variability in Humoral Immunity to Measles Vaccine: New Developments. *Trends Mol. Med.* **21**, 789–801 (2015).

25. J. W. Glasser, Z. Feng, S. B. Omer, P. J. Smith, L. E. Rodewald, The effect of heterogeneity in uptake of the measles, mumps, and rubella vaccine on the potential for outbreaks of measles: a modelling study. *Lancet Infect. Dis.* **16**, 599–605 (2016).

26. S. Nyathi, H. C. Karpel, K. L. Sainani, Y. Maldonado, P. J. Hotez, E. Bendavid, N. C. Lo, The 2016 California policy to eliminate nonmedical vaccine exemptions and changes in vaccine coverage: An empirical policy analysis. *PLoS Med.* **16**, e1002994 (2019).

27. M. J. Mina, T. Kula, Y. Leng, M. Li, R. D. de Vries, M. Knip, H. Siljander, M. Rewers, D. F. Choy, M. S. Wilson, H. B. Larman, A. N. Nelson, D. E. Griffin, R. L. de Swart, S. J. Elledge, Measles virus infection diminishes preexisting antibodies that offer protection from other pathogens. *Science* **366**, 599–606 (2019).

28. V. N. Petrova, B. Sawatsky, A. X. Han, B. M. Laksono, L. Walz, E. Parker, K. Pieper, C. A. Anderson, R. D. de Vries, A. Lanzavecchia, P. Kellam, V. von Messling, R. L. de Swart, C. A. Russell, Incomplete genetic reconstitution of B cell pools contributes to prolonged immunosuppression after measles. *Sci Immunol* **4**, eaay6125 (2019).

29. M. Ferren, B. Horvat, C. Mathieu, Measles Encephalitis: Towards New Therapeutics. *Viruses* **11** (2019).

30. P. A. Rota, W. J. Moss, M. Takeda, R. L. de Swart, K. M. Thompson, J. L. Goodson, Measles. *Nat. Rev. Dis. Primers* **2**, 16049 (2016).

31. M. A. Brindley, S. Chaudhury, R. K. Plemper, Measles virus glycoprotein complexes preassemble intracellularly and relax during transport to the cell surface in preparation for fusion. *J. Virol.* **89**, 1230–1241 (2015).

32. R. L. de Swart, S. Yüksel, A. D. M. E. Osterhaus, Relative contributions of measles virus hemagglutinin- and fusion protein-specific serum antibodies to virus neutralization. *J. Virol.* **79**, 11547–11551 (2005).

33. M. A. Muñoz-Alía, J. M. Casasnovas, M. L. Celma, J. Carabaña, P. B. Liton, R. Fernandez-Muñoz, Measles Virus Hemagglutinin epitopes immunogenic in natural infection and vaccination are targeted by broad or genotype-specific neutralizing monoclonal antibodies. *Virus Res.* **236**, 30–43 (2017).

34. R. L. de Swart, S. Yüksel, C. N. Langerijs, C. P. Muller, A. D. M. E. Osterhaus, Depletion of measles virus glycoprotein-specific antibodies from human sera reveals genotype-specific neutralizing antibodies. *J. Gen. Virol.* **90**, 2982–2989 (2009).

35. C. Richardson, D. Hull, P. Greer, K. Hasel, A. Berkovich, G. Englund, W. Bellini, B. Rima, R. Lazzarini, The nucleotide sequence of the mRNA encoding the fusion protein of measles virus (Edmonston strain): a comparison of fusion proteins from several different paramyxoviruses. *Virology* **155**, 508–523 (1986).

36. Y. Yanagi, M. Takeda, S. Ohno, T. Hashiguchi, Measles virus receptors. *Curr. Top. Microbiol. Immunol.* **329**, 13–30 (2009).

37. T. Hashiguchi, K. Maenaka, Y. Yanagi, Measles virus hemagglutinin: structural insights into cell entry and measles vaccine. *Front. Microbiol.* **2**, 247 (2011).

38. H. Tatsuo, N. Ono, K. Tanaka, Y. Yanagi, SLAM (CDw150) is a cellular receptor for measles virus. *Nature* **406**, 893–897 (2000).

39. M. D. Mühlebach, M. Mateo, P. L. Sinn, S. Prüfer, K. M. Uhlig, V. H. J. Leonard, C. K. Navaratnarajah, M. Frenzke, X. X. Wong, B. Sawatsky, S. Ramachandran, P. B. McCray Jr, K. Cichutek, V. von Messling, M. Lopez, R. Cattaneo, Adherens junction protein nectin-4 is the epithelial receptor for measles virus. *Nature* **480**, 530–533 (2011).

40. R. S. Noyce, D. G. Bondre, M. N. Ha, L.-T. Lin, G. Sisson, M.-S. Tsao, C. D. Richardson, Tumor cell marker PVRL4 (nectin 4) is an epithelial cell receptor for measles virus. *PLoS Pathog.* **7**, e1002240 (2011).

41. H. S. Yin, R. G. Paterson, X. Wen, R. A. Lamb, T. S. Jardetzky, "Structure of the uncleaved ectodomain of the paramyxovirus (hPIV3) fusion protein" (PNAS, 2005); https://doi.org/10.1073/pnas.0503989102.

42. R. A. Lamb, R. G. Paterson, T. S. Jardetzky, Paramyxovirus membrane fusion: lessons from the F and HN atomic structures. *Virology* **344**, 30–37 (2006).

43. G. B. E. Stewart-Jones, G.-Y. Chuang, K. Xu, T. Zhou, P. Acharya, Y. Tsybovsky, L. Ou, B. Zhang, B. Fernandez-Rodriguez, V. Gilardi, C. Silacci-Fregni, M. Beltramello, U. Baxa, A. Druz, W.-P. Kong, P. V. Thomas, Y. Yang, K. E. Foulds, J.-P. Todd, H. Wei, A. M. Salazar, D. G. Scorpio, B. Carragher, C. S. Potter, D. Corti, J. R. Mascola, A. Lanzavecchia, P. D. Kwong, Structure-based design of a quadrivalent fusion glycoprotein vaccine for human parainfluenza virus types 1–4. *Proceedings of the National Academy of Sciences* **115**, 12265–12270 (2018).

44. S. C. Harrison, Viral membrane fusion. *Nat. Struct. Mol. Biol.* **15**, 690–698 (2008).

45. A. Chang, R. E. Dutch, Paramyxovirus fusion and entry: multiple paths to a common end. *Viruses* **4**, 613–636 (2012).

46. R. K. Plemper, M. A. Brindley, R. M. Iorio, Structural and mechanistic studies of measles virus illuminate paramyxovirus entry. *PLoS Pathog.* **7**, e1002058 (2011).

47. J. M. White, S. E. Delos, M. Brecher, K. Schornberg, Structures and mechanisms of viral membrane fusion proteins: multiple variations on a common theme. *Crit. Rev. Biochem. Mol. Biol.* **43**, 189–219 (2008).

48. A. Sapir, O. Avinoam, B. Podbilewicz, L. V. Chernomordik, Viral and developmental cell fusion mechanisms: conservation and divergence. *Dev. Cell* **14**, 11–21 (2008).

49. C. Mathieu, M. Ferren, O. Harder, F. T. Bovier, T. C. Marcink, C. Predella, F. Angius, J. Drew-Bear, N. V. Dorrello, A. L. Greninger, A. Moscona, S. Niewiesk, B. Horvat, M. Porotto, Single-chain variable fragment antibody constructs neutralize measles virus infection in vitro and in vivo. *Cell. Mol. Immunol.* **18**, 1835–1837 (2021).

50. E. Malvoisin, F. Wild, Contribution of measles virus fusion protein in protective immunity: anti-F monoclonal antibodies neutralize virus infectivity and protect mice against challenge. *J. Virol.* **64**, 5160–5162 (1990).

51. A. Sun, A. Prussia, W. Zhan, E. E. Murray, J. Doyle, L.-T. Cheng, J.-J. Yoon, E. V. Radchenko, V. A. Palyulin, R. W. Compans, D. C. Liotta, R. K. Plemper, J. P. Snyder, Nonpeptide inhibitors of measles virus entry. *J. Med. Chem.* **49**, 5080–5092 (2006).

52. T. Hashiguchi, Y. Fukuda, R. Matsuoka, D. Kuroda, M. Kubota, Y. Shirogane, S. Watanabe, K. Tsumoto, D. Kohda, R. K. Plemper, Y. Yanagi, Structures of the prefusion form of measles virus fusion protein in complex with inhibitors. *Proc. Natl. Acad. Sci. U. S. A.* **115**, 2496–2501 (2018).

53. F. T. Bovier, K. Rybkina, S. Biswas, O. Harder, T. C. Marcink, S. Niewiesk, A. Moscona, C. A. Alabi, M. Porotto, Inhibition of Measles Viral Fusion Is Enhanced by Targeting Multiple Domains of the Fusion Protein. *ACS Nano* **15**, 12794–12803 (2021).

54. S. Niewiesk, P.-G. Germann, Development of neutralizing antibodies correlates with resolution of interstitial pneumonia after measles virus infection in cotton rats. *J. Exp. Anim. Sci.* **40**, 201–210 (2000).

55. S. Niewiesk, Cotton rats (Sigmodon hispidus): an animal model to study the pathogenesis of measles virus infection. *Immunol. Lett.* **65**, 47–50 (1999).

56. C. K. Navaratnarajah, S. Kumar, A. Generous, S. Apte-Sengupta, M. Mateo, R. Cattaneo, The measles virus hemagglutinin stalk: structures and functions of the central fusion activation and membrane-proximal segments. *J. Virol.* **88**, 6158–6167 (2014).

57. P. Plattet, L. Alves, M. Herren, H. C. Aguilar, Measles Virus Fusion Protein: Structure, Function and Inhibition. *Viruses* **8**, 112 (2016).

58. Y. H. Kim, J. E. Donald, G. Grigoryan, G. P. Leser, A. Y. Fadeev, R. A. Lamb, W. F. DeGrado, Capture and imaging of a prehairpin fusion intermediate of the paramyxovirus PIV5. *Proc. Natl. Acad. Sci. U. S. A.* **108**, 20992–20997 (2011).

59. A. Talekar, A. Moscona, M. Porotto, Measles virus fusion machinery activated by sialic acid binding globular domain. *J. Virol.* **87**, 13619–13627 (2013).

60. E. M. Jurgens, C. Mathieu, L. M. Palermo, D. Hardie, B. Horvat, A. Moscona, M. Porotto, Measles fusion machinery is dysregulated in neuropathogenic variants. *MBio* **6** (2015).

61. C. D. Richardson, A. Scheid, P. W. Choppin, Specific inhibition of paramyxovirus and myxovirus replication by oligopeptides with amino acid sequences similar to those at the N-termini of the F1 or HA2 viral polypeptides. *Virology* **105**, 205–222 (1980).

62. F. Angius, H. Smuts, K. Rybkina, D. Stelitano, B. Eley, J. Wilmshurst, M. Ferren, A. Lalande, C. Mathieu, A. Moscona, B. Horvat, T. Hashiguchi, M. Porotto, D. Hardie, Analysis of a Subacute Sclerosing Panencephalitis Genotype B3 Virus from the 2009-2010 South African Measles Epidemic Shows That Hyperfusogenic F Proteins Contribute to Measles Virus Infection in the Brain. *J. Virol.* **93** (2019).

63. C. Mathieu, F. T. Bovier, M. Ferren, N. A. P. Lieberman, C. Predella, A. Lalande, V. Peddu, M. J. Lin, A. Addetia, A. Patel, V. Outlaw, B. Corneo, N. V. Dorrello, T. Briese, D. Hardie, B. Horvat, A. Moscona, A. L. Greninger, M. Porotto, Molecular Features of the Measles Virus Viral Fusion Complex That Favor Infection and Spread in the Brain. *MBio* **12**, e0079921 (2021).

64. M. N. Ha, S. Delpeut, R. S. Noyce, G. Sisson, K. M. Black, L.-T. Lin, D. Bilimoria, R. K. Plemper, G. G. Privé, C. D. Richardson, Mutations in the Fusion Protein of Measles Virus That Confer Resistance to the Membrane Fusion Inhibitors Carbobenzoxy-d-Phe-l-Phe-Gly and 4-Nitro-2-Phenylacetyl Amino-Benzamide. *J. Virol.* **91** (2017).

65. K. Swanson, X. Wen, G. P. Leser, R. G. Paterson, R. A. Lamb, T. S. Jardetzky, Structure of the Newcastle disease virus F protein in the post-fusion conformation. *Virology* **402**, 372–379 (2010).

66. A. J. May, K. R. Pothula, K. Janowska, P. Acharya, Structures of Langya Virus Fusion Protein Ectodomain in Pre- and Postfusion Conformation. *J. Virol.* **97**, e0043323 (2023).

67. L. Chen, J. J. Gorman, J. McKimm-Breschkin, L. J. Lawrence, P. A. Tulloch, B. J. Smith, P. M. Colman, M. C. Lawrence, The structure of the fusion glycoprotein of Newcastle disease virus suggests a novel paradigm for the molecular mechanism of membrane fusion. *Structure* **9**, 255–266 (2001).

68. P. O. Byrne, B. E. Fisher, D. R. Ambrozak, E. G. Blade, Y. Tsybovsky, B. S. Graham, J. S. McLellan, R. J. Loomis, Structural basis for antibody recognition of vulnerable epitopes on Nipah virus F protein. *Nat. Commun.* **14**, 1494 (2023).

69. T. A. Poor, L. M. Jones, A. Sood, G. P. Leser, M. D. Plasencia, D. L. Rempel, T. S. Jardetzky, R. J. Woods, M. L. Gross, R. A. Lamb, Probing the paramyxovirus fusion (F) protein-refolding event from pre- to postfusion by oxidative footprinting. *Proc. Natl. Acad. Sci. U. S. A.* **111**, E2596-605 (2014).

70. M. A. Riddell, J. S. Rota, P. A. Rota, Review of the temporal and geographical distribution of measles virus genotypes in the prevaccine and postvaccine eras. *Virol. J.* **2**, 87 (2005).

71. P. A. Rota, W. J. Bellini, Update on the global distribution of genotypes of wild type measles viruses. *J. Infect. Dis.* **187 Suppl 1**, S270-6 (2003).

72. Nomenclature for describing the genetic characteristics of wild-type measles viruses (update). Part I. *Wkly. Epidemiol. Rec.* **76**, 242–247 (2001).

73. Genetic analysis of measles virus (2022). https://www.cdc.gov/measles/lab-tools/genetic-analysis.html.

74. R. D. de Vries, S. McQuaid, G. van Amerongen, S. Yüksel, R. J. Verburgh, A. D. M. E. Osterhaus, W. P. Duprex, R. L. de Swart, Measles immune suppression: lessons from the macaque model. *PLoS Pathog.* **8**, e1002885 (2012).

75. H. V. Dang, Y.-P. Chan, Y.-J. Park, J. Snijder, S. C. Da Silva, B. Vu, L. Yan, Y.-R. Feng, B. Rockx, T. W. Geisbert, C. E. Mire, C. C. Broder, D. Veesler, An antibody against the F glycoprotein inhibits Nipah and Hendra virus infections. *Nat. Struct. Mol. Biol.* **26**, 980–987 (2019).

76. V. A. Avanzato, K. Y. Oguntuyo, M. Escalera-Zamudio, B. Gutierrez, M. Golden, S. L. Kosakovsky Pond, R. Pryce, T. S. Walter, J. Seow, K. J. Doores, O. G. Pybus, V. J. Munster, B. Lee, T. A. Bowden, A structural basis for antibody-mediated neutralization of Nipah virus reveals a site of vulnerability at the fusion glycoprotein apex. *Proc. Natl. Acad. Sci. U. S. A.* **116**, 25057–25067 (2019).

77. H. V. Dang, R. W. Cross, V. Borisevich, Z. A. Bornholdt, B. R. West, Y.-P. Chan, C. E. Mire, S. C. Da Silva, A. S. Dimitrov, L. Yan, M. Amaya, C. K. Navaratnarajah, L. Zeitlin, T. W. Geisbert, C. C. Broder, D. Veesler, Broadly neutralizing antibody cocktails targeting Nipah virus and Hendra virus fusion glycoproteins. *Nat. Struct. Mol. Biol.* **28**, 426–434 (2021).

78. T. C. Marcink, G. Zipursky, W. Cheng, K. Stearns, S. Stenglein, K. Golub, F. Cohen, F. Bovier, D. Pfalmer, A. L. Greninger, M. Porotto, A. des Georges, A. Moscona, Subnanometer structure of an enveloped virus fusion complex on viral surface reveals new entry mechanisms. *Sci Adv* **9**, eade2727 (2023).

79. M. Cabán, J. V. Rodarte, M. Bibby, M. D. Gray, J. J. Taylor, M. Pancera, J. Boonyaratanakornkit, Cross-protective antibodies against common endemic respiratory viruses. *Nat. Commun.* **14**, 798 (2023).

80. L. L. Hammitt, R. Dagan, Y. Yuan, M. Baca Cots, M. Bosheva, S. A. Madhi, W. J. Muller, H. J. Zar, D. Brooks, A. Grenham, U. Wählby Hamrén, V. S. Mankad, P. Ren, T. Takas, M. E. Abram, A. Leach, M. P. Griffin, T. Villafana, MELODY Study Group, Nirsevimab for prevention of RSV in healthy late-preterm and term infants. *N. Engl. J. Med.* **386**, 837–846 (2022).

81. H. Wu, D. S. Pfarr, S. Johnson, Y. A. Brewah, R. M. Woods, N. K. Patel, W. I. White, J. F. Young, P. A. Kiener, Development of motavizumab, an ultra-potent antibody for the prevention of respiratory syncytial virus infection in the upper and lower respiratory tract. *J. Mol. Biol.* **368**, 652–665 (2007).

82. Q. Zhu, J. S. McLellan, N. L. Kallewaard, N. D. Ulbrandt, S. Palaszynski, J. Zhang, B. Moldt, A. Khan, C. Svabek, J. M. McAuliffe, D. Wrapp, N. K. Patel, K. E. Cook, B. W. M. Richter, P. C. Ryan, A. Q. Yuan, J. A. Suzich, A highly potent extended half-life antibody as a potential RSV vaccine surrogate for all infants. *Sci. Transl. Med.* **9**, eaaj1928 (2017).

83. O. Reynard, C. Gonzalez, C. Dumont, M. Iampietro, M. Ferren, S. Le Guellec, L. Laurie, C. Mathieu, G. Carpentier, G. Roseau, F. T. Bovier, Y. Zhu, D. Le Pennec, J. Montharu, A. Addetia, A. L. Greninger, C. A. Alabi, E. Brisebard, A. Moscona, L. Vecellio, M. Porotto, B. Horvat, Nebulized fusion inhibitory peptide protects cynomolgus macaques from measles virus infection. *Nat. Commun.* **13**, 6439 (2022).

84. C. Mathieu, D. Huey, E. Jurgens, J. C. Welsch, I. DeVito, A. Talekar, B. Horvat, S. Niewiesk, A. Moscona, M. Porotto, Prevention of measles virus infection by intranasal delivery of fusion inhibitor peptides. *J. Virol.* **89**, 1143–1155 (2015).

85. G. Frey, H. Peng, S. Rits-Volloch, M. Morelli, Y. Cheng, B. Chen, A fusion-intermediate state of HIV-1 gp41 targeted by broadly neutralizing antibodies. *Proc. Natl. Acad. Sci. U. S. A.* **105**, 3739–3744 (2008).

86. F. H. Niesen, H. Berglund, M. Vedadi, The use of differential scanning fluorimetry to detect ligand interactions that promote protein stability. *Nat. Protoc.* **2**, 2212–2221 (2007).

87. P. J. A. Cock, T. Antao, J. T. Chang, B. A. Chapman, C. J. Cox, A. Dalke, I. Friedberg, T. Hamelryck, F. Kauff, B. Wilczynski, M. J. L. de Hoon, Biopython: freely available Python tools for computational molecular biology and bioinformatics. *Bioinformatics* **25**, 1422–1423 (2009).

88. F. Sievers, D. G. Higgins, Clustal omega. *Curr. Protoc. Bioinformatics* **48**, 3.13.1-3.13.16 (2014).

89. J. Pei, N. V. Grishin, AL2CO: calculation of positional conservation in a protein sequence alignment. *Bioinformatics* **17**, 700–712 (2001).

90. Hunter, Matplotlib: A 2D Graphics Environment. **9**, 90–95 (2007).

91. M. Waskom, seaborn: statistical data visualization. *J. Open Source Softw.* **6**, 3021 (2021).

92. T. D. Goddard, C. C. Huang, E. C. Meng, E. F. Pettersen, G. S. Couch, J. H. Morris, T. E. Ferrin, UCSF ChimeraX: Meeting modern challenges in visualization and analysis. *Protein Sci.* **27**, 14–25 (2018).

93. A. Punjani, J. L. Rubinstein, D. J. Fleet, M. A. Brubaker, cryoSPARC: algorithms for rapid unsupervised cryo-EM structure determination. *Nat. Methods* **14**, 290–296 (2017).

94. S. H. W. Scheres, RELION: implementation of a Bayesian approach to cryo-EM structure determination. *J. Struct. Biol.* **180**, 519–530 (2012).

95. D. Kimanius, L. Dong, G. Sharov, T. Nakane, S. H. W. Scheres, New tools for automated cryo-EM single-particle analysis in RELION-4.0. *Biochem. J* **478**, 4169–4185 (2021).

96. D. Zyla, *Dzyla/Follow_Relion_gracefully: V4* (2023; https://zenodo.org/record/7844516).

97. S. Q. Zheng, E. Palovcak, J.-P. Armache, K. A. Verba, Y. Cheng, D. A. Agard, MotionCor2: anisotropic correction of beam-induced motion for improved cryo-electron microscopy. *Nat. Methods* **14**, 331–332 (2017).

98. A. Rohou, N. Grigorieff, CTFFIND4: Fast and accurate defocus estimation from electron micrographs. *J. Struct. Biol.* **192**, 216–221 (2015).

99. T. Bepler, A. Morin, M. Rapp, J. Brasch, L. Shapiro, A. J. Noble, B. Berger, Positive-unlabeled convolutional neural networks for particle picking in cryo-electron micrographs. *Nat. Methods* **16**, 1153–1160 (2019).

100. M. Mirdita, K. Schütze, Y. Moriwaki, L. Heo, S. Ovchinnikov, M. Steinegger, ColabFold: making protein folding accessible to all. *Nat. Methods* **19**, 679–682 (2022).

101. J. Jumper, R. Evans, A. Pritzel, T. Green, M. Figurnov, O. Ronneberger, K. Tunyasuvunakool, R. Bates, A. Žídek, A. Potapenko, A. Bridgland, C. Meyer, S. A. A. Kohl, A. J. Ballard, A. Cowie, B. Romera-Paredes, S. Nikolov, R. Jain, J. Adler, T. Back, S. Petersen, D. Reiman, E. Clancy, M. Zielinski, M. Steinegger, M. Pacholska, T. Berghammer, S. Bodenstein, D. Silver, O. Vinyals, A. W. Senior, K. Kavukcuoglu, P. Kohli, D. Hassabis, Highly accurate protein structure prediction with AlphaFold. *Nature* **596**, 583–589 (2021).

102. P. Emsley, B. Lohkamp, W. G. Scott, K. Cowtan, Features and development of Coot. *Acta Crystallogr. D Biol. Crystallogr.* **66**, 486–501 (2010).

103. J. Agirre, M. Atanasova, H. Bagdonas, C. B. Ballard, A. Baslé, J. Beilsten-Edmands, R. J. Borges, D. G. Brown, J. J. Burgos-Mármol, J. M. Berrisford, P. S. Bond, I. Caballero, L. Catapano, G. Chojnowski, A. G. Cook, K. D. Cowtan, T. I. Croll, J. É. Debreczeni, N. E. Devenish, E. J. Dodson, T. R. Drevon, P. Emsley, G. Evans, P. R. Evans, M. Fando, J. Foadi, L. Fuentes-Montero, E. F. Garman, M. Gerstel, R. J. Gildea, K. Hatti, M. L. Hekkelman, P. Heuser, S. W. Hoh, M. A. Hough, H. T. Jenkins, E. Jiménez, R. P. Joosten, R. M. Keegan, N. Keep, E. B. Krissinel, P. Kolenko, O. Kovalevskiy, V. S. Lamzin, D. M. Lawson, A. A. Lebedev, A. G. W. Leslie, B. Lohkamp, F. Long, M. Malý, A. J. McCoy, S. J. McNicholas, A. Medina, C. Millán, J. W. Murray, G. N. Murshudov, R. A. Nicholls, M. E. M. Noble, R. Oeffner, N. S. Pannu, J. M. Parkhurst, N. Pearce, J. Pereira, A. Perrakis, H. R. Powell, R. J. Read, D. J. Rigden, W. Rochira, M. Sammito, F. Sánchez Rodríguez, G. M. Sheldrick, K. L. Shelley, F. Simkovic, A. J. Simpkin, P. Skubak, E. Sobolev, R. A. Steiner, K. Stevenson, I. Tews, J. M. H. Thomas, A. Thorn, J. T. Valls, V. Uski, I. Usón, A. Vagin, S. Velankar, M. Vollmar, H. Walden, D. Waterman, K. S. Wilson, M. D. Winn, G. Winter, M. Wojdyr, K. Yamashita, The CCP4 suite: integrative software for macromolecular crystallography. *Acta Crystallogr D Struct Biol* **79**, 449–461 (2023).

104. T. C. Terwilliger, S. J. Ludtke, R. J. Read, P. D. Adams, P. V. Afonine, Improvement of cryo-EM maps by density modification. *Nat. Methods* **17**, 923–927 (2020).

105. P. D. Adams, P. V. Afonine, G. Bunkóczi, V. B. Chen, I. W. Davis, N. Echols, J. J. Headd, L.-W. Hung, G. J. Kapral, R. W. Grosse-Kunstleve, A. J. McCoy, N. W. Moriarty, R. Oeffner, R. J. Read, D. C. Richardson, J. S. Richardson, T. C. Terwilliger, P. H. Zwart, PHENIX: a comprehensive Python-

based system for macromolecular structure solution. *Acta Crystallogr. D Biol. Crystallogr.* **66**, 213–221 (2010).

106. E. Krissinel, K. Henrick, “Detection of Protein Assemblies in Crystals” in *Computational Life Sciences* (Springer Berlin Heidelberg, 2005), pp. 163–174.

107. B. O. Forsberg, P. N. M. Shah, A. Burt, A robust normalized local filter to estimate compositional heterogeneity directly from cryo-EM maps. *Nat. Commun.* **14**, 5802 (2023).

108. N. Guex, M. C. Peitsch, T. Schwede, Automated comparative protein structure modeling with SWISS-MODEL and Swiss-PdbViewer: a historical perspective. *Electrophoresis* **30 Suppl 1**, S162-73 (2009).

109. T. I. Croll, ISOLDE: a physically realistic environment for model building into low-resolution electron-density maps. *Acta Crystallogr. D Struct. Biol.* **74**, 519–530 (2018).

110. C. S. Hughes, S. Moggridge, T. Müller, P. H. Sorensen, G. B. Morin, J. Krijgsveld, Single-pot, solid-phase-enhanced sample preparation for proteomics experiments. *Nat. Protoc.* **14**, 68–85 (2019).

111. W. Peng, V. Rayaprolu, A. D. Parvate, M. F. Pronker, S. Hui, D. Parekh, K. Shaffer, X. Yu, E. O. Saphire, J. Snijder, Glycan shield of the ebolavirus envelope glycoprotein GP. *Commun. Biol.* **5**, 785 (2022).

112. P. Virtanen, R. Gommers, T. E. Oliphant, M. Haberland, T. Reddy, D. Cournapeau, E. Burovski, P. Peterson, W. Weckesser, J. Bright, S. J. van der Walt, M. Brett, J. Wilson, K. J. Millman, N. Mayorov, A. R. J. Nelson, E. Jones, R. Kern, E. Larson, C. J. Carey, İ. Polat, Y. Feng, E. W. Moore, J. VanderPlas, D. Laxalde, J. Perktold, R. Cimrman, I. Henriksen, E. A. Quintero, C. R. Harris, A. M. Archibald, A. H. Ribeiro, F. Pedregosa, P. van Mulbregt, SciPy 1.0 Contributors, SciPy 1.0: fundamental algorithms for scientific computing in Python. *Nat. Methods* **17**, 261–272 (2020).

113. W. Mc Kinney, Pandas: A foundational python library for data analysis and statistics (2011). https://www.dlr.de/sc/portaldata/15/resources/dokumente/pyhpc2011/submissions/pyhpc2011_submission_9.pdf.

114. F. Charlier, M. Weber, D. Izak, E. Harkin, M. Magnus, J. Lalli, L. Fresnais, M. Chan, N. Markov, O. Amsalem, S. Proost, A. Krasoulis, getzze, S. Repplinger, *Trevismd/Statannotations: V0.5* (2022; https://zenodo.org/record/7213391).

Science
AAAS

Supplementary Materials for

A neutralizing antibody prevents post-fusion transition of measles fusion protein

Dawid S. Zyla[1], Roberta Della Marca[2,3,4], Gele Niemeyer[1,5], Gillian Zipursky[2,3], Kyle Stearns[2,3], Cameron Leedale[6], Elizabeth B. Sobolik[7], Heather Callaway[1#], Chitra Hariharan[1], Weiwei Peng[8,9], Diptiben Parekh[1], Tara C. Marcink[2,3], Ruben Diaz Avalos[1], Branka Horvat[10], Cyrille Mathieu[11], Joost Snijder[8,9], Alexander L. Greninger[7], Kathryn M. Hastie[1], Stefan Niewiesk[6], Anne Moscona[2,3,12,13], Matteo Porotto[2,3,4*], Erica Ollmann Saphire[1,14*]

Corresponding authors: mp3509@columbia.edu and erica@lji.org

The PDF file includes:

Figs. S1 to S12

Tables S1 to S5

Other Supplementary Materials for this manuscript include the following:

Movie S1

Supplementary figures

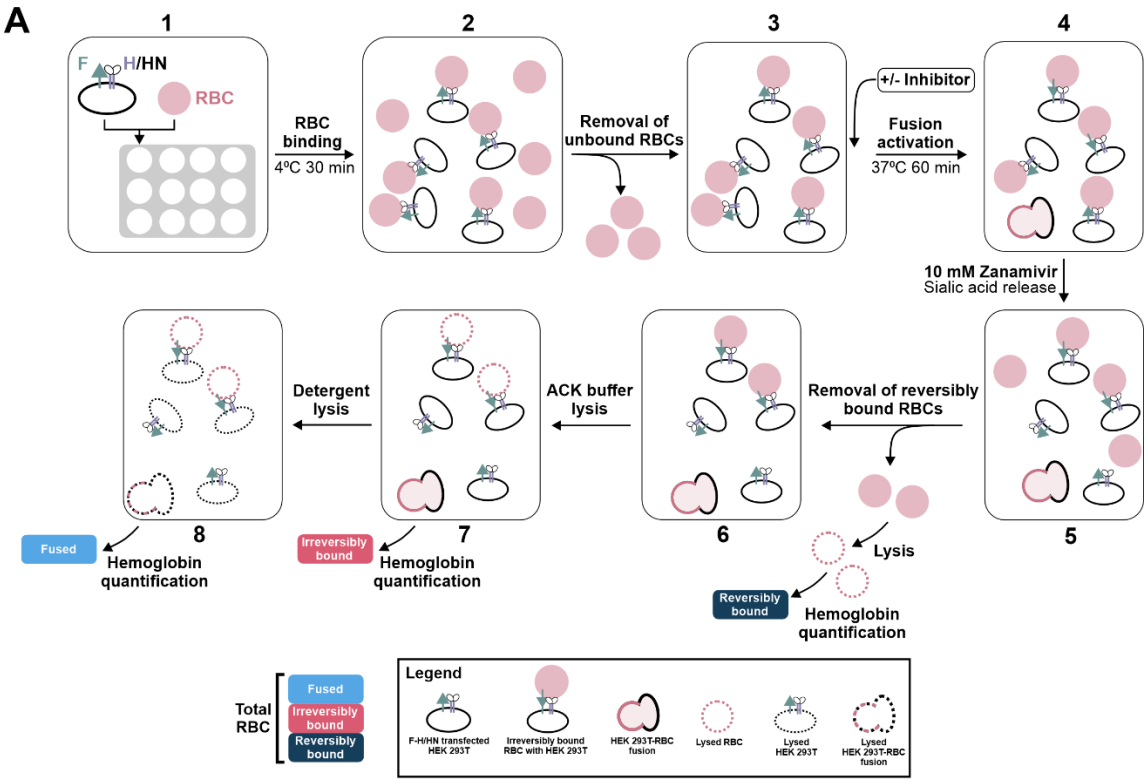

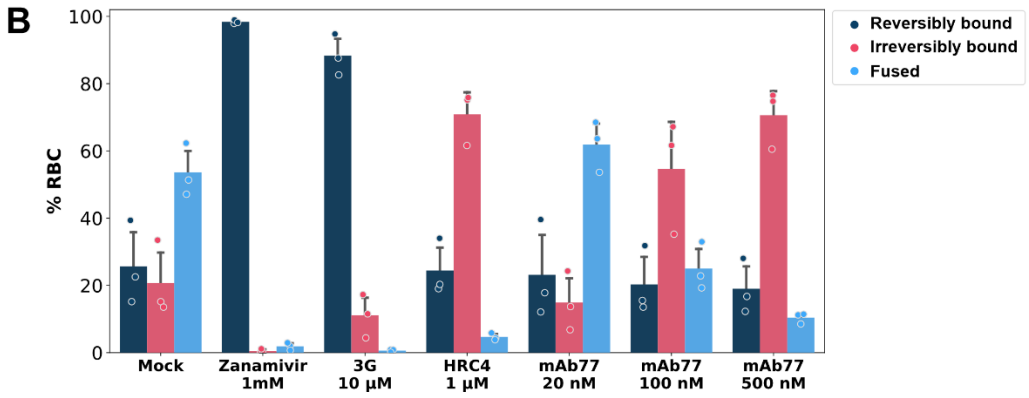

Figure S1. RBC fusion assay overview and non-normalized assay data.

A) Detailed RBC fusion assay schematic related to Fig. 2A following steps described in the Methods section.

B) Detailed plot from Fig. 2B showing the non-normalized average percentages (± std dev) and individual data points for reversibly bound, irreversibly bound, or fused RBCs following treatment with diluent (Mock), inhibitors, or mAb 77 (20-500 nM).

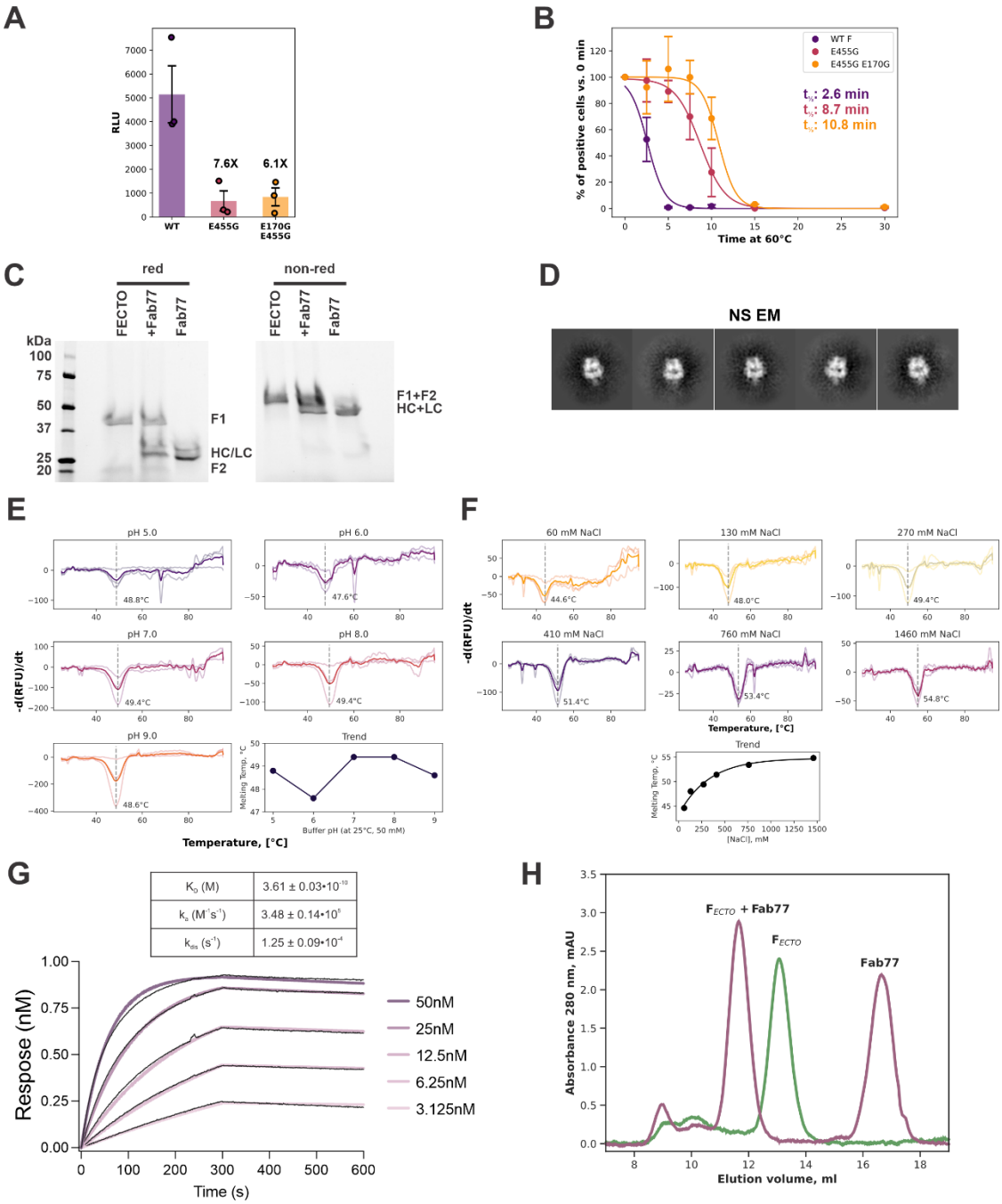

1430 ***Figure S2. Biochemical analyses of F_{ECTO} and mAb 77 Fab complex formation.***

A) The β-galactosidase complementation assay between cells expressing MeV H and F variants and cells
1432 expressing the MeV receptor huCD150 showed that after an 18-hour incubation period, E455G and E455G/E170G had 7.6-fold and 6.1-fold lower fusogenicity, respectively, compared to the wild-type
1434 (wt) F protein. Bars represent mean, and error bars correspond to standard error.

B) A time-based thermal stability assay was performed on F variants expressed on cells by evaluating the
1436 binding of mAb77. Cells expressing F variants were incubated at 60 °C for varying periods ranging from 0 to 30 minutes. A higher percentage of mAb 77 epitope was observed in cells expressing E455G

1438 and E455G/E170G than those expressing wt F. The stability half-lives were 8.7 and 10.8 minutes for E455G and E455G/E170G, respectively, compared to 2.6 minutes for wt protein. Points correspond to
1440 mean, and error bars show standard error.

C) Purity of F_{ECTO} and Fab 77 verified using SDS-PAGE. F_{ECTO} exhibits a single band corresponding to
1442 approximately 54 kDa (F1+F2) and 37 kDa under non-reducing (non-red) conditions and reducing conditions (red), respectively. Due to its high glycosylation, F2 appears as a smear at around 20 kDa.

1444 D) Negative stain electron microscopy (NS EM) 2D classes of F_{ECTO} in the pre-fusion conformation after purification.

1446 E) Effect of buffer pH on F_{ECTO} apparent melting temperature (T_m^{app}). Five different pH values were examined, with the resulting F_{ECTO} T_m^{app} values measured and depicted in the corresponding graphs. The
1448 final plot shows the trend across the pH values.

F) Effect of salt concentration on F_{ECTO} stability. F_{ECTO} was incubated in six salt concentrations (60 – 1460
1450 mM) and the stability is expressed as T_m^{app}. The trend demonstrating the relationship between salt concentration and F_{ECTO} stability is illustrated in the final graph.

1452 G) Bio-Layer interferometry (BLI) binding curves for F_{ECTO} and Fab 77 reveal high association ($3.48 \cdot 10^5$ $M^{-1}s^{-1}$) and slow dissociation kinetics ($1.25 \cdot 10^{-4}$ s^{-1}), with a calculated K_D of $3.61 \cdot 10^{-10}$ M.

1454 H) Size exclusion profile of the F_{ECTO} and Fab 77 complex. The purple line signifies a 1:1 mixture of F_{ECTO}: Fab 77, with a fully formed complex peak at approximately 11.7 ml and a Fab peak at 16.5 ml. The
1456 green line represents the F_{ECTO} elution profile.

1458

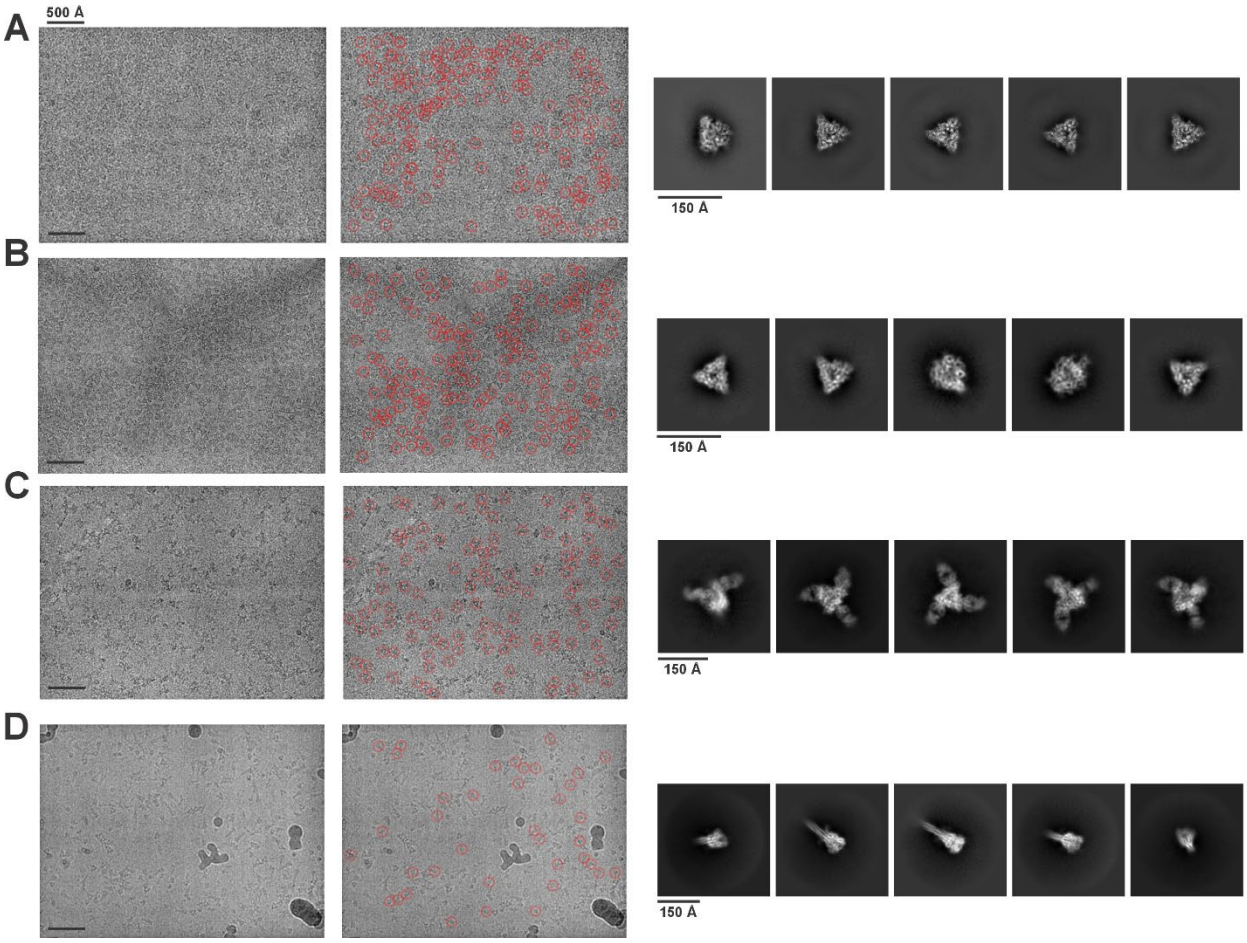

Figure S3 Representative micrographs for each dataset with particle picking from the final particle stack (left) and selected 2D classes (right).

A) $F_{ECTO,}$ B) F_{ECTO}-[FIP-HRC]$_2$-PEG$_{11}$, C) F_{ECTO}-Fab 77, D) F_{ECTO} in post-fusion conformation. Scale bar (left) for the micrographs corresponds to 500 Å. Red circles show particles locations that contributed to the final particle stack. The scale bar (right) corresponds to 150 Å.

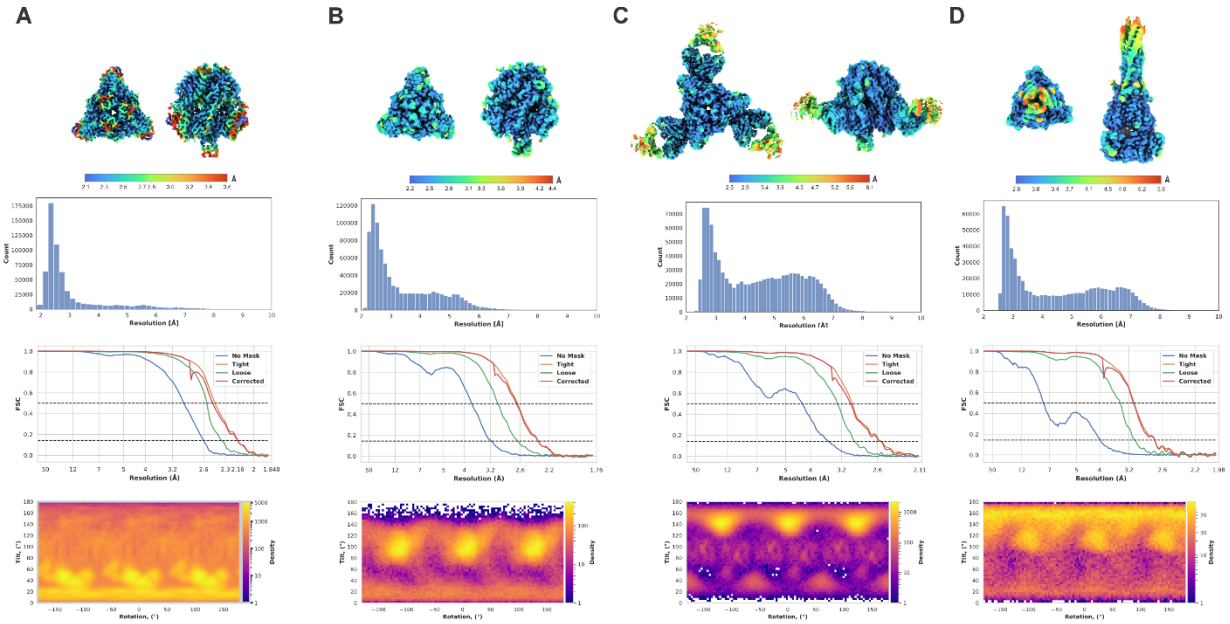

Figure S4 Final map quality, local resolution, FSC, and particle angular distribution for each recorded dataset.

A) F_{ECTO}
B) F_{ECTO}-[FIP-HRC]$_2$-PEG$_{11}$
C) F_{ECTO}-Fab 77
D) F_{ECTO} in post-fusion conformation.

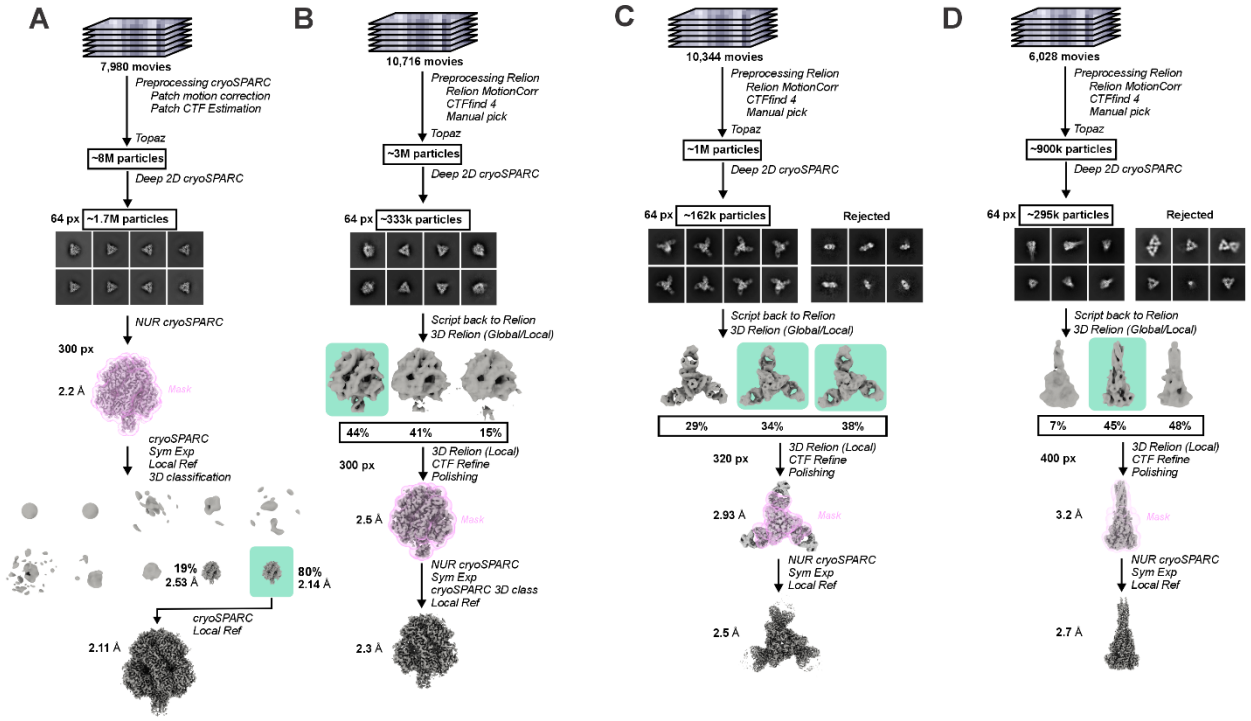

Figure S5 Cryo-EM data processing for each recorded dataset as described in the Methods. The green highlight indicates selected classes.

E) F_{ECTO}

F) F_{ECTO}-$[FIP\text{-}HRC]_2$-PEG_{11}

G) F_{ECTO}-Fab 77

H) F_{ECTO} in post-fusion conformation.

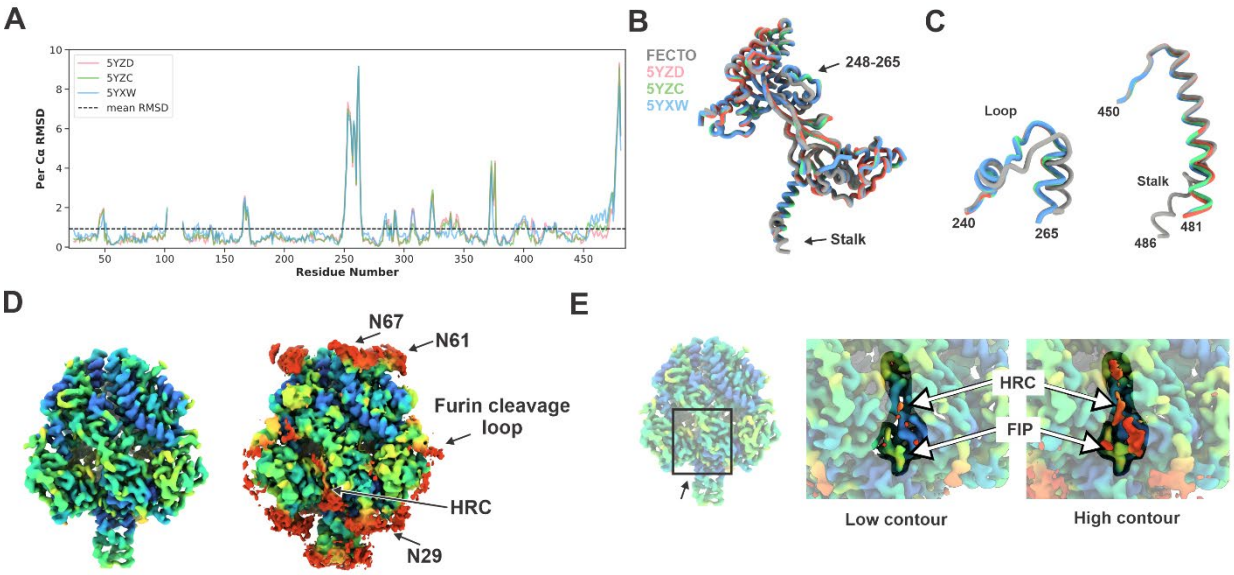

Figure S6. Structure analysis and comparison of F_{ECTO}.

A) Differences between disulfide-stabilized F_{ECTO} (X-ray), and native F_{ECTO} (cryo-EM). The graph shows the Cα root mean square deviation (RMSD) between the X-ray structures (F_{ECTO} APO: 5YXW, F_{ECTO} FIP: 5YZD, F_{ECTO} AS-48: 5YZC) and the cryo-EM F_{ECTO}. Each model was globally aligned based on a single monomer (F1+F2), after which the RMSD was calculated between residues present in both structures. Regions with the highest RMSD include the loop 248-265 and the stalk region highlighted in B and C.

B) The ribbon diagram presents the global alignment of the X-ray and cryo-EM models, as in C. Arrows indicated areas exhibiting high RMSD.

C) Close-up view of the areas marked in D), with the starting and ending residues indicated. The color coding matches that in D).

D) Application of local scaling to the F_{ECTO}-$[FIP\text{-}HRC]_2$-PEG_{11} map using OccuPy. On the left, the relative occupancy of the unsharpened map is shown, and on the right, an equalized map that enhances regions with low occupancy or resolution, illustrating glycans (N29, N61, and N67), the furin-containing loop and the density from $[FIP\text{-}HRC]_2$-PEG_{11}. Color map corresponding to the calculated local scale, red indicating low values and blue indicating high values.

E) The equalized map is presented at both low (on the left) and high (on the right) contour levels. Arrows indicate locations of FIP and HRC. The density corresponding to FIP was clearly visible in the unequalized map, whereas the density associated with HRC only became apparent at the high contour level in the equalized map.

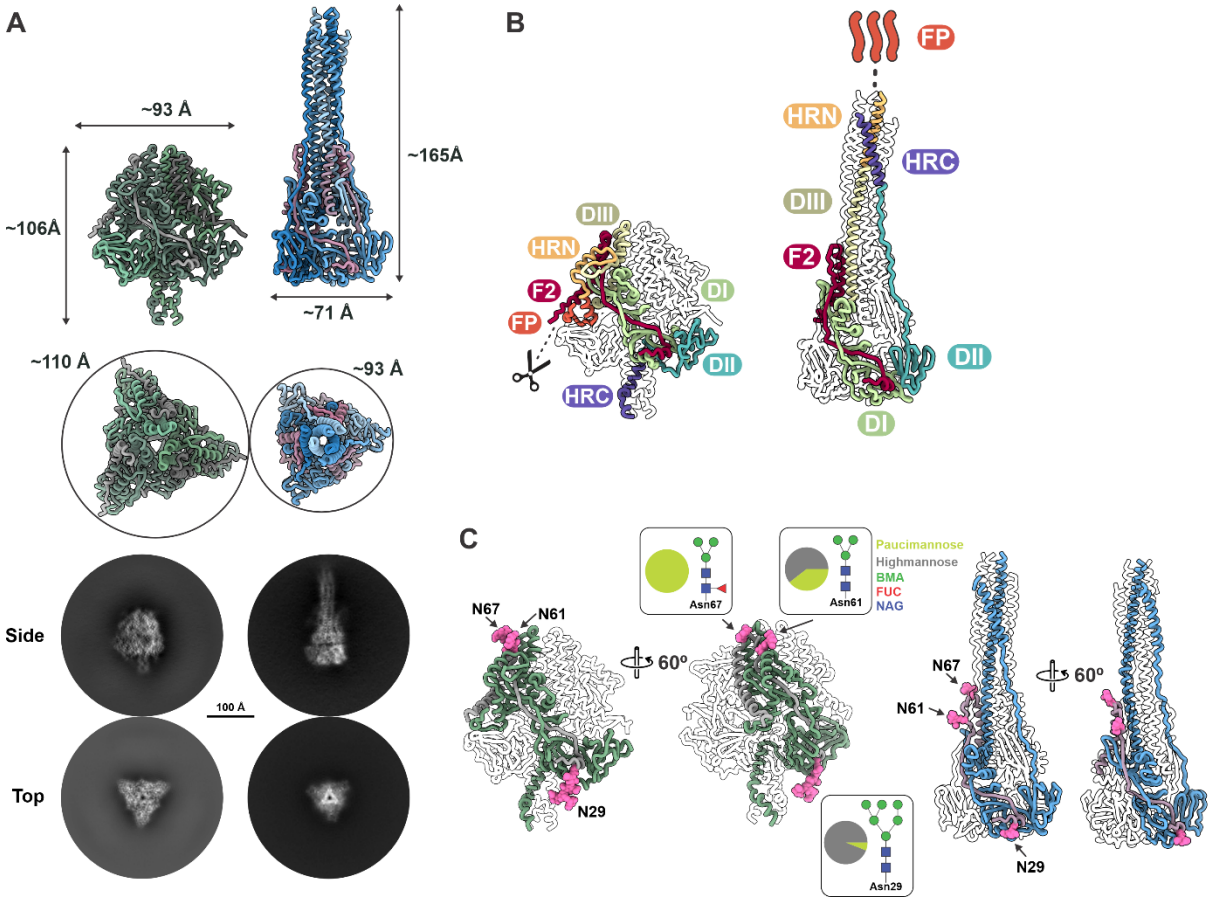

1506 ***Figure S7. Comparative analysis of the shape and dimensions of F_{ECTO} in its pre- and post-fusion conformations.***

1508 A) Final models for both F_{ECTO} conformations and their respective dimensions (top). The final map projections (bottom) reveal differences in particle shapes between the two conformations when viewed
1510 from the side and top. The scale bar represents 100 Å.

B) Visual representation of the domains, elucidating the changes in domain conformations and overall
1512 shape transitioning from the pre- to post-fusion state. The domains are color-coded consistently across both models for ease of comparison.

1514 C) Glycosylation analysis of F_{ECTO}: MeV F has three glycosylation sites at positions N29, N61, and N67 (hot pink). The observed glycosylation patterns from mass spectrometry correspond to the expected
1516 glycosylation patterns obtained from the *Drosophila* S2 expression system. Specifically, the N29 site was found to have a uniform high-mannose type of glycosylation, while N61 mostly and N67 uniformly
1518 had paucimannose type of glycosylation. The modeled glycosylation sites are shown for pre-fusion F_{ECTO} (left, green/gray) and post-fusion F_{ECTO} (right, blue-dark pink). NAG: N-Acetylglucosamine,
1520 FUC: Fucose, BMA: beta-D-mannose.

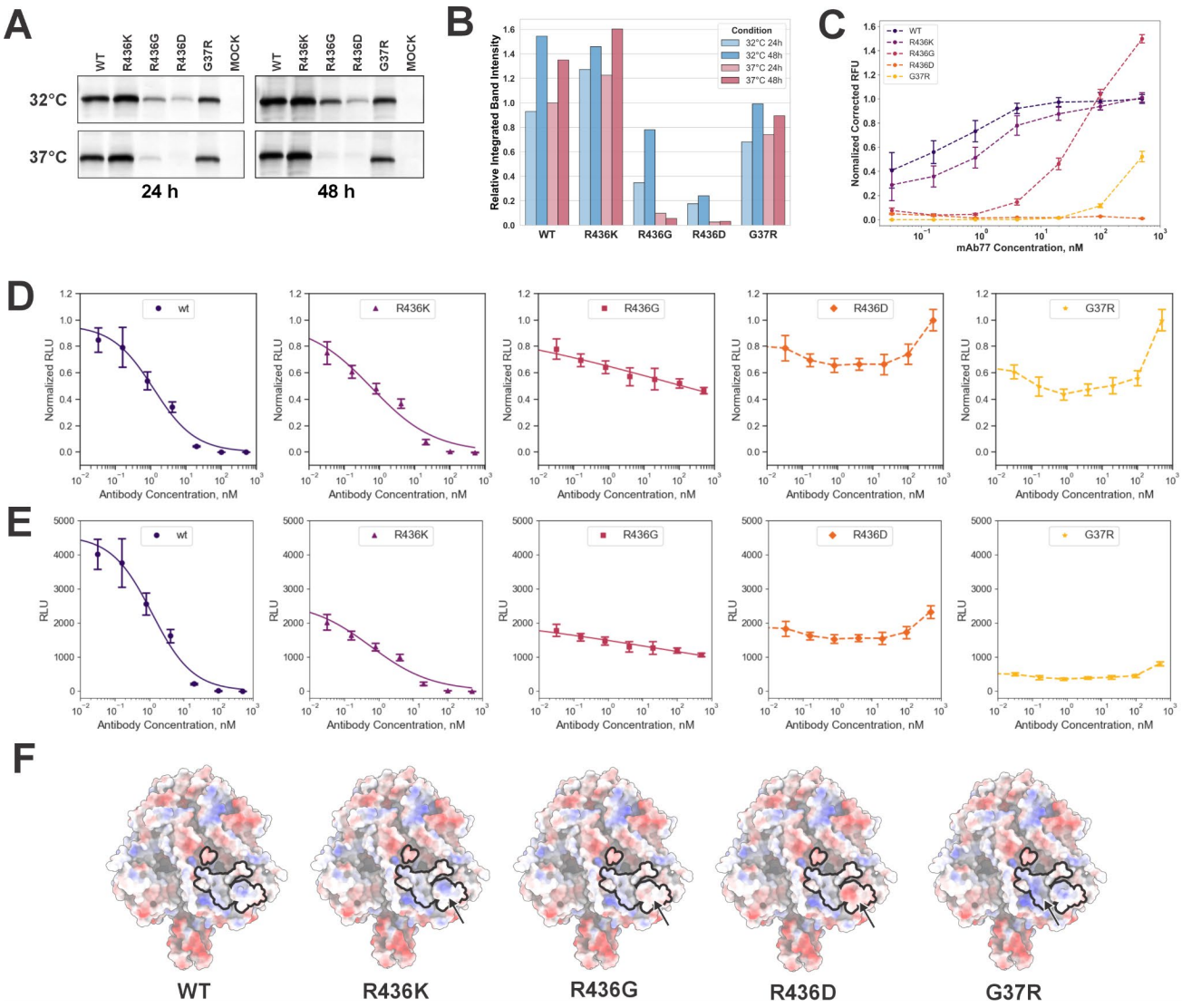

1522 ***Figure S8. Quantitative analysis of cell-surface expression, cell-surface staining and fusion inhibition of F protein variants by mAb 77.***

1524 A) Western blot analysis using anti-HRC antibodies to detect F protein variants after 24h and 48h in cell-surface biotinylation assays conducted at 32 °C and 37 °C.

1526 B) Bar graph representing the relative integrated band intensities derived from A). The data are normalized with respect to the wt F protein band intensity at 24 h, 37 °C. Longer expression (48 h) led to higher
1528 levels of F for all variants except R436G at 37 °C. Also, a change in charge (R436G) or charge reversal (R436D) lowered the amount of protein detected on the surface.

1530 C) Cell surface staining of F protein variants after 48 h at 32 °C in the presence of mAb 77, adjusted for average expression levels as determined from panel B. Dotted lines connect discrete data points for
1532 clarity. The binding of mAb 77 to the R436K variant of F was only slightly lower than that for wt. Despite the lower expression of R436G, after normalizing expression levels binding of mAb 77 had
1534 enhanced higher recognition of this construct relative to wild type, albeit with much lower affinity.

D) F protein variant fusion inhibition by mAb 77 was examined at 32 °C using the β-galactosidase complementation assay. Data are normalized to the highest signal per variant. Solid lines represent nonlinear regression logistic curves fit to the data, whereas dotted lines connect discrete data points for ease of interpretation. Fit values were obtained from global fits to all data points with shared IC_{50} and Hill slope wt: IC_{50}=1.2±0.3 nM, slope=0.73±0.11, R436K: IC_{50}=0.58±0.27 nM, slope=0.48±0.08, R436G: IC_{50}=65.7±41.7 nM, slope=0.12±0.02. Error bars represent standard error from 3 biological replicates.

E) As in panel D, but non-normalized data are shown to elucidate the relative magnitude of fusion activity among different F protein variants. Even in the absence of mAb77-induced inhibition, the G37R mutation had only ~12% of the fusion capability seen for wt F, indicating that MeV harboring this F variant would likely have lower propagation potential.

F) Computational analysis of the impact of point mutations on the electrostatic surface potential maps of F_{ECTO}. The color scale represents electrostatic potential in volts, with red, white and blue indicating -10, 0, and +10, respectively. Arrows pinpoint the locations of mutations under investigation. The R436K mutation does not modify the local charge within the mAb 77 epitope on the F protein, which accounts for the wild-type-like performance of this variant in the mAb77 inhibition assay. In contrast, the R436G mutation leads to a loss of charge, significantly reducing the binding and neutralization capacity of mAb77, although it does not prevent recognition of the F protein by mAb77. The introduction of a charge reversal mutation, R436D, induces charge repulsion with Asp109 in the heavy chain CDR 3 of mAb 77, which is likely responsible for the complete lack of mAb 77 binding to this variant. Furthermore, the G37R mutation may introduce steric hindrance within the indicated area, particularly affecting interactions with Y54 in the heavy chain CDR 2 that could impact binding.

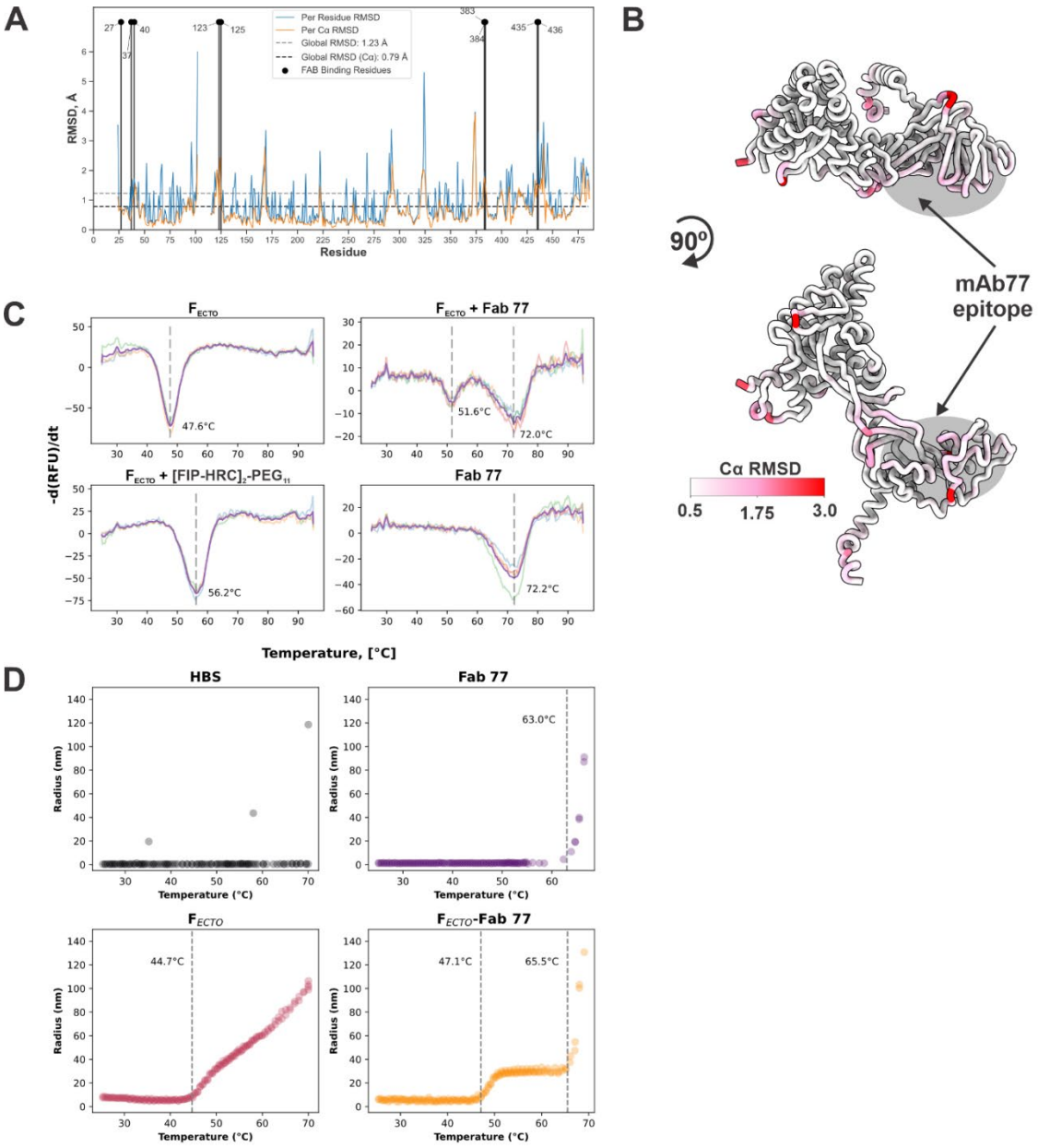

Figure S9. Structural and biophysical investigation of the effects of mAb 77 on F_{ECTO}.

A) Per residue RMSD analysis between F_{ECTO}-Fab 77 and F_{ECTO} structure. Two RMSD statistics per residue were calculated based on all atoms in the residue (blue) and only between Cα (orange). Black dots positioned on top of the lines indicate the locations of residues involved in the mAb 77 epitope. Dashed lines represent the average all-atom (gray) and C-alpha atom (Cα, black) RMSD.

B) The influence of Fab 77 binding is demonstrated through structural mapping of the Cα RMSD between two pre-fusion F_{ECTO} structures in complex with Fab 77 and F_{ECTO} alone. The intensifying red gradient indicates an increase in Cα RMSD, with arrows pinpointing the antibody-binding epitope presented in gray.

C) Differential scanning fluorimetry (DSF) experiments with F_{ECTO} and complexes of F_{ECTO} with [FIP-HRC]$_2$-PEG$_{11}$ and Fab 77. The thermal stability of F_{ECTO}, stabilized by two point mutations (E170G and E450G), had a T_m^{app} of 47.6 °C. The addition of [FIP-HRC]$_2$-PEG$_{11}$ enhanced the thermal stability to 56.7 °C, whereas the Fab 77 only slightly stabilized F_{ECTO}, raising the temperature to 51.6 °C.

D) Temperature-resolved Dynamic Light Scattering (DLS) experiment with F_{ECTO} and Fab 77. The experiment reveals the unique behavior of F_{ECTO} in the presence and absence of Fab 77. In the absence of Fab 77, F_{ECTO} undergoes a transition at 44.7 °C, which increases the particle radius concurrent with increased temperature. The absence of a clear lag phase following triggering suggests that refolding and aggregation occur simultaneously. However, when F_{ECTO} is bound by Fab 77, a distinct plateau phase emerges between approximately 50-65 °C, indicating stabilization of an intermediate refolding step. The unfolding/aggregation behavior of Fab 77 alone and in the F_{ECTO}-Fab 77 complex is similar, starting above 63 °C. Due to experimental limitations, the Fab 77 trace is not fully resolved at temperatures higher than 70 °C. Onset (10% of the total signal) is indicated by dashed lines.

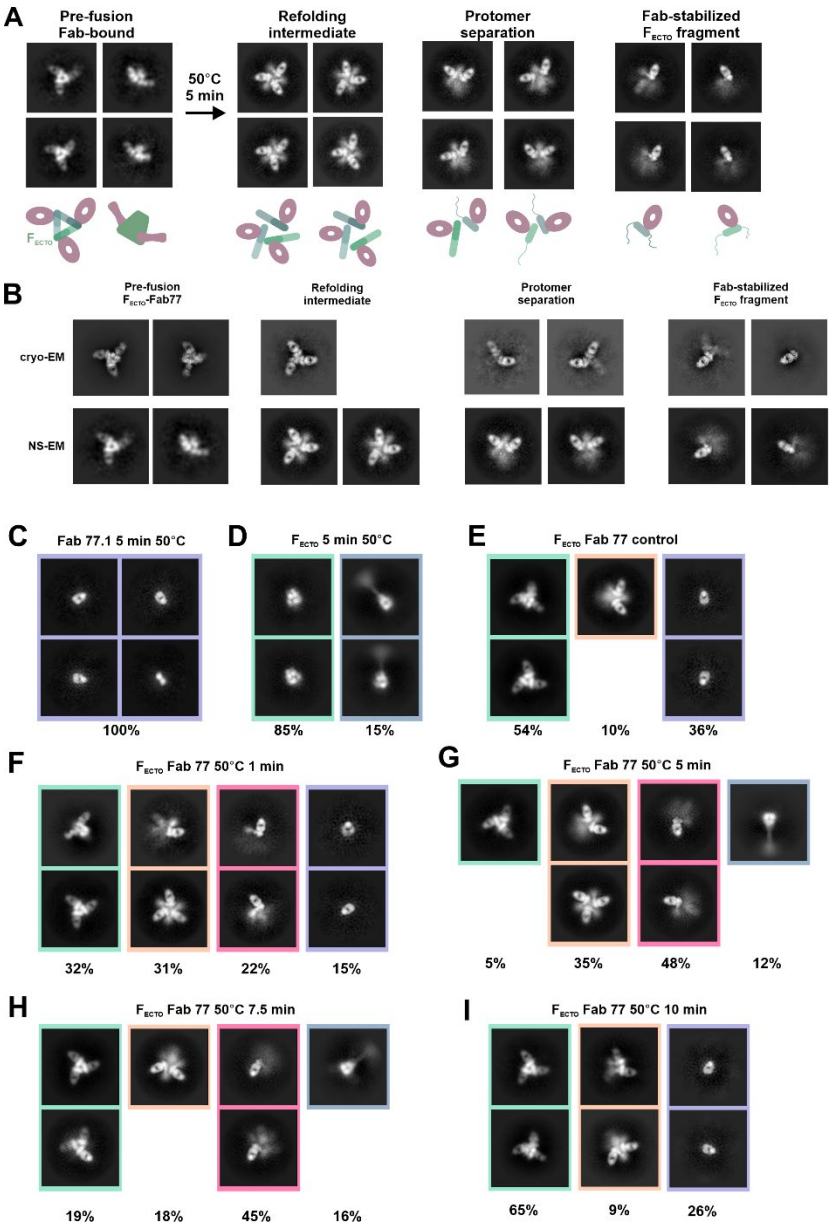

Figure S10. Time-resolved heating experiment with F_{ECTO}-Fab 77.

A) 2D Classification and simplified schematic of NS EM heating experiment with the FECTO-Fab 77 complex. The F_{ECTO}-Fab 77 complex was heated for 5 min at 50 °C, followed by rapid cooling on ice and preparation of NS EM grids. 2D classification analysis revealed heterogeneous conformations of the F_{ECTO}-Fab 77 complex.

B) A comparison between the 2D classes obtained from cryo-EM and NS EM experiments shows a good agreement between the two techniques in terms of particle morphology and conformation.

C, D) 5-min, 50° C heat-treated controls for Fab 77 and F_{ECTO}.

E) Unheated control for the F_{ECTO}-Fab 77 complex.

F, G, H, I) Time-resolved thermal analysis of F_{ECTO}-Fab 77. The most representative or the sole class obtained during the 2D classification round is shown. As indicated in Fig S11A, all datasets were processed using identical parameters regarding micrograph pre-processing, particle picking, and 2D classification. The states that were obtained are color-coded: violet: Fab 77, green: F_{ECTO}/F_{ECTO}-Fab 77 in pre-fusion conformation, slate blue: F_{ECTO} in post-fusion conformation, orange: relaxed/open state of F_{ECTO}-Fab 77, red: Fab-stabilized F_{ECTO} fragment.

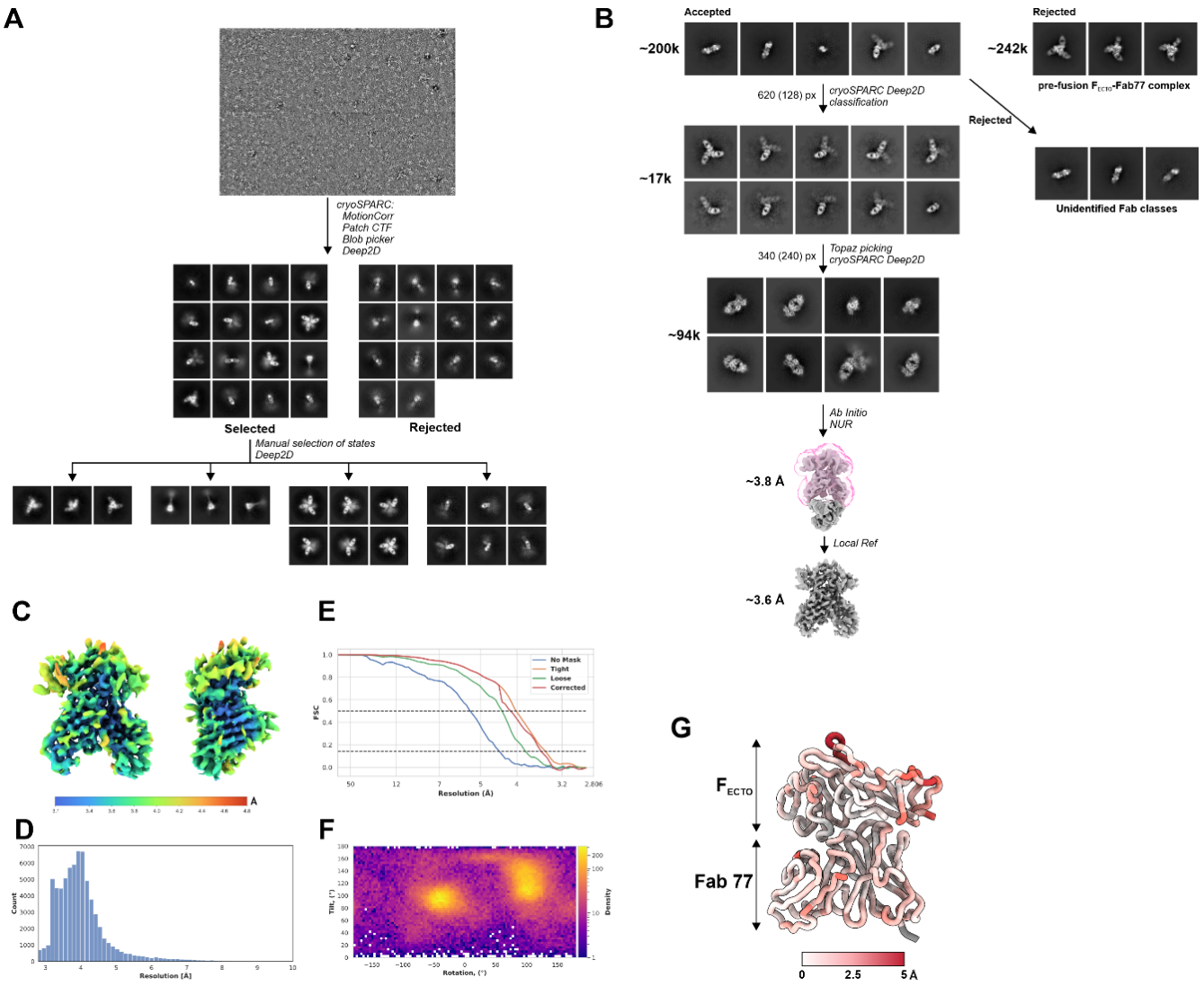

1598 ***Figure S11. Processing workflow and statistics for the Fab 77-F_{ECTO} fragment and refolding intermediates.***

1600 A) General processing workflow for NS EM datasets.

B) Cryo-EM processing workflow for the Fab 77-F_{ECTO} fragment.

1602 C, D, E, F) Local resolution, local resolution histogram, FSC, and angular distribution of the final Fab 77-F_{ECTO} fragment map.

1604 G) Cα RMSD between F_{ECTO}-Fab 77 structure and Fab 77-stabilized F_{ECTO} fragment shows minor changes of the F_{ECTO} epitope upon glycoprotein separation. The intensifying red gradient indicates an increase
1606 in Cα RMSD, with arrows pinpointing F and Fab regions.

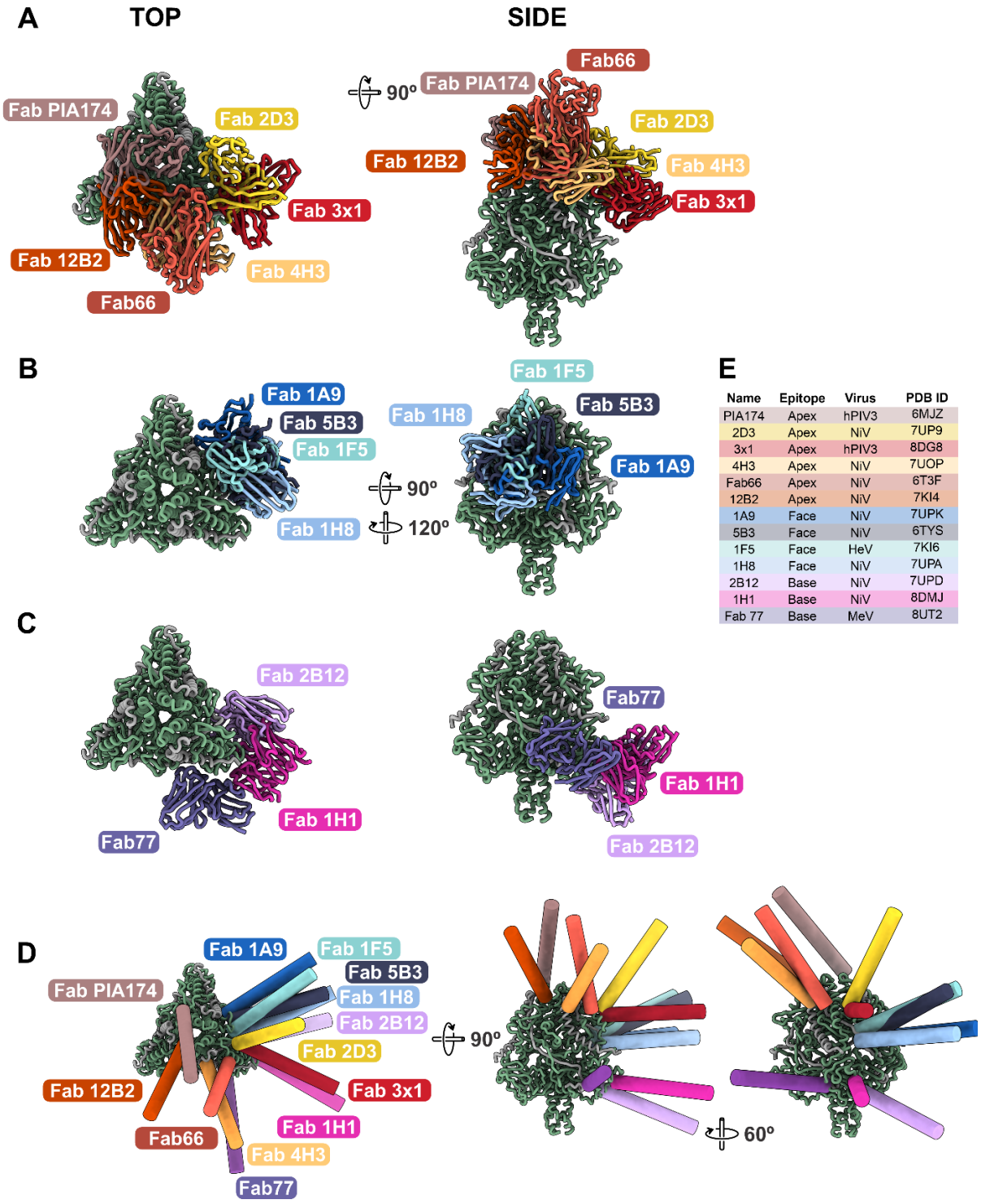

1608 ***Figure S12. Distinguishing three main epitopes among 12 antibodies that target the paramyxovirus F protein.***

1610 A) Apex binding antibodies (Fab PIA174: 6MJZ, Fab 12B2: 7KI4, Fab66: 6T3F, Fab 4H3: 7UOP, Fab 3x1: 8DG8, Fab 2D3: 7UP9) recognize the top part of domain III and F2.

B) Face binding antibodies (Fab 1A9: 7UPK, Fab 5B3: 6TYS, Fab 1F5: 7KI6, Fab 1H8: 7UPA) mainly target domain I and the lower part of domain III.

C) Base binding antibodies (Fab 2B12: 7UPD, Fab 1H1: 7UPB, Fab 77: this study) primarily bind domain II, the bottom of domain I and the linker region between domain II and HRC. Interestingly, Fab 1H1 also recognizes the post-fusion conformation of Nipah F.

D) Approach angles of antibodies included in A-C. Each axis was determined based on the long dimension of a whole Fab structure fitting into the available Fab fragment. Axes are colored based on the antibody colors from A-E) Summary table with all the antibodies discussed and their epitope and corresponding viral targets. The abbreviations are as follows: hPIV: Human Parainfluenza Virus, NiV: Nipah Virus, HeV: Hendra Virus, MeV: Measles Virus.

Tables

Table S1. Model and map statistics.

Model **PDB ID** **EMDB ID**	**F_{ECTO}-Fab 77** **8UT2** **EMD-42527**	**F_{ECTO} post-fusion** **8UTF** **EMD-42539**	**F_{ECTO}-(FIP-HRC4)$_2$-PEG11** **8UUQ** **EMD-42595**	**F_{ECTO}** **8UUP** **EMD-42593**	**Fab 77-F_{ECTO} fragment** **9AT8** **EMD-43827 / EMD-43828**
Composition (#)					
Chains	16	11	13	10	5
Atoms	16159 (Hydrogens: 0)	9894 (Hydrogens: 0)	10768 (Hydrogens: 0)	10729 (Hydrogens: 0)	3088 (Hydrogens: 0)
Residues	Protein: 2037	Protein: 1256	Protein: 1357	Protein: 1357 Nucleotide: 0	Protein: 396 Nucleotide: 0
Water	229	134	33	105	0
Ligands	BMA: 6 NAG: 15	NAG: 9	LIG: 3 NAG: 15 BMA: 6 MAN: 4	BMA: 6 NAG: 15	NAG: 1
Model statistics					
Bonds (RMSD)					
Length (Å) (# > 4sigma)	0.003 (0)	0.002 (0)	0.006 (0)	0.002 (0)	0.002 (0)
Angles (°) (# > 4sigma)	0.548 (0)	0.525 (0)	0.685 (1)	0.523 (0)	0.535 (0)
MolProbity score	1.55	1.25	1.14	1.12	1.91
Clash score	6.47	4.88	3.53	3.27	9.22
Ramachandran plot (%)					
Outliers	0.20	0.00	0.00	0.00	0.00
Allowed	2.98	1.21	1.71	1.64	6.44
Favored	96.82	98.79	98.29	98.36	93.56
Rama-Z (Ramachandran plot Z-score, RMSD)					
whole (N = 2013)	-0.60 (0.18)	0.25 (0.23)	-0.08 (0.21)	0.44 (0.22)	-1.97 (0.41)
helix (N = 429)	0.23 (0.24)	1.10 (0.23)	0.14 (0.23)	1.01 (0.23)	--- (---)
sheet (N = 486)	-0.06 (0.24)	1.23 (0.48)	0.25 (0.35)	0.24 (0.37)	-1.29 (0.47)
loop (N = 1098)	-0.77 (0.18)	-0.86 (0.23)	-0.13 (0.22)	-0.08 (0.22)	-1.36 (0.37)
Rotamer outliers (%)	0.00	0.00	0.00	0.00	0.00
Cbeta outliers (%)	NA	NA	NA	NA	NA
Peptide plane (%)					
Cis proline/general	7.7/0.2	0.0/0.0	0.0/0.0	0.0/0.0	5.9/0.0
Twisted proline/general	0.0/0.0	0.0/0.0	0.0/0.0	0.0/0.0	0.0/0.0
CaBLAM outliers (%)	1.96	0.79	0.90	0.68	4.74
ADP (B-factors)					
Iso/Aniso (#)	16159/0	9894/0	10768/0	10729/0	3088/0
min/max/mean					
Protein	7.78/145.94/55.27	0.00/196.59/75.85	14.91/124.73/48.03	9.78/127.18/41.02	7.19/116.77/33.72
Ligand	27.94/156.21/78.74	102.93/151.05/126.78	0.20/171.70/57.90	-0.00/104.16/50.63	66.91/66.91/66.91
Water	13.74/72.27/39.79	33.21/102.23/55.55	23.07/53.29/37.59	15.04/47.76/29.70	---
Occupancy					
Mean	1.00	1.00	1.00	1.00	1.00
Data					
Box					
Supplied Resolution (Å)	2.6	2.7	2.3	2.11	3.8
Resolution Estimates (Å)	Masked/(Unmasked)	Masked/(Unmasked)	Masked/(Unmasked)	Masked/(Unmasked)	Masked/(Unmasked)
d FSC (half maps; 0.143) (Å)	2.56	2.72	2.34	2.11	3.6
d model	2.9/(3.0)	3.1/(3.1)	2.6/(2.6)	2.4/(2.5)	3.5/(3.5)
d FSC model (0/0.143/0.5) (Å)	2.5/2.5/2.8/ (2.5/2.6/3.0)	2.6/2.7/3.0 (2.7/2.7/3.1)	2.2/2.3/2.5 (2.3/2.3/2.7)	2.1/2.1/2.3 2.1/2.2/2.4	2.8/3.4/3.7 2.8/3.4/3.7
Map min/max/mean	2.73/3.40/0.03	4.28/6.60/0.04	2.73/4.58/0.03	2.30/3.15/0.00	-7.32/11.44/0.08
Model vs. Data					
CC (mask)	0.81	0.82	0.89	0.72	0.69
CC (box)	0.69	0.67	0.72	0.58	0.62
CC (peaks)	0.67	0.65	0.72	0.58	0.56
CC (volume)	0.79	0.80	0.87	0.71	0.67
Mean CC for ligands	0.65	0.54	0.64	0.68	0.51
Data acquisition					
Microscope / camera	Thermo Titan Krios G3 300kV / Gatan K3 + GIF Bioquantum				
Magnification	130'000 X				
Exposure / total electron exposure	2.5 s / ~50 e$^-$/Å^2			2 s / 70 e$^-$/Å^2	2.5 s / ~50 e$^-$/Å^2
Frames	50				
Defocus range	-0.6-2.5 µm				
Pixel size (raw/final) (Å)	0.66 / 1.056	0.66 / 0.99	0.66 / 0.88	0.66 / 0.92	0.66 / 1.403
Number of micrographs (all/final)	10344 / 7798	6028 / 5420	10716 / 5830	7980 / 7965	10344 / 7798
Number of particles (unique / symmetry expanded)	142852 / 428556	52850 / 158562	100661 / 235003	354182 / 454125	94848 / -
Box size (raw/final) (px)	512 / 320	600 / 400	400 / 300	420/300	340 / 160
Symmetry	Local C1 from symmetry expanded C3				C1

Table S2. mAb 77-F interface statistics per chain.

Interface	Interface area (Å^2)	ΔG (kcal/mol)	Hydrogen bonds	Salt bridges
HC-F1'	466	-2	7	1

HC-F2'	283	-4	4	0
HC-F1”	140	-1.5	2	0
LC-F1”	106	-1.1	2	0
Total	995	-8.6	15	1

1628

Table S3. CRD regions of mAb 77 involved in F binding.

CDR	Residue range	Interactions
CDR H-1	31-36	4
CDR H-2	51-66	3
CDR H-3	99-110	7
CDR L-2	69-75	2

1630

1632

Table S4. Hydrogen bonds and salt bridges between mAb 77 and F at the

HC CDR 3 $F1_A$ Interface

Hydrogen bond	HC residue [atom]	Distance (Å)	F1' residue [atom]
1	TRP 101 [N]	3.08	GLN 383 [OE1]
2	TYR 107 [OH]	2.38	ARG 435 [O]
3	TYR 107 [OH]	3.5	ARG 435 [N]
4	TYR 107 [O]	2.9	ARG 436 [NH1]
5	TYR 105 [O]	2.96	ARG 436 [NH1]
6	ASP 109 [OD1]	2.74	ARG 436 [NH2]

Salt bridge	HC residue [atom]	Distance (Å)	F1' residue [atom]
1	ASP 109 [OD2]	2.97	ARG 436 [NH2]

HC CDR 1 $F1_A$ Interface

Hydrogen bond	HC residue [atom]	Distance (Å)	F1' residue [atom]
7	ASP 32 [OD2]	2.5	GLN 383 [N]
8	TYR 33 [OH]	3.54	GLY 384 [N]

HC CDR 1 $F1_B$ Interface

Hydrogen bond	HC residue [atom]	Distance (Å)	F1" residue [atom]
13	TYR 27 [OH]	3.12	LEU 123 [O]
14	SER 31 [O]	3.46	VAL 125 [N]

HC CDR 2 $F2_A$ Interface

Hydrogen bond	HC residue [atom]	Distance (Å)	F2' residue [atom]
9	TYR 54 [OH]	3.22	GLY 37 [O]
10	ARG 72 [NH2]*	3	SER 40 [O]

11	THR 55 [OG1]	3.41	TRP 27 [NE1]
12	THR 57 [OG1]	3.75	TRP 27 [NE1]

*not part of CDR-H2

LC CDR 2 $F1_A$ Interface

Hydrogen bond	LC residue [atom]	Distance (Å)	F1" residue [atom]
15	TYR 49 [OH]	3.14	ARG 435 [N]
16	GLN 55 [OE1]	2.99	SER 434 [OG]

Table S5. Residue variants present in the mAb 77 epitope.

Residue Position[a]	Original Residue	Residue Variation	Interaction Type	Total interactions
27	W	-	Sidechain	2
37	**G (99.88%)**	**R (0.12%)**	**Backbone**	**1**
40	S	-	Sidechain/Backbone	1
123	L	-	Backbone	1
125	V	-	Backbone	1
383	Q	-	Sidechain/Backbone	2
384	G	-	Backbone	1
434	S	-	Sidechain/Backbone	3
435	R	-	Backbone	3
436	**R (72.89%)**	**K (27.11%)**	**Sidechain**	**3**

[a]Variant residues shown in bold were tested for their effect on mAb 77 binding.

Movies

Movies S1. A model morph between F_{ECTO} pre-fusion and post-fusion models shows the movement of domains with respect to domain I.